**İSTANBUL TECHNICAL UNIVERSITY ★ INSTITUTE OF SCIENCE AND TECHNOLOGY**

# CUSP ENERGETIC PARTICLES: A CASE STUDY FOR PARTICLE TRACING

**M.Sc. Thesis by**

**Altansuvd BOLD**

**Department :** **Meteorological Engineering**

**Programme:** **Meteorological Engineering**

**JUNE 2007**

**İSTANBUL TECHNICAL UNIVERSITY ★ INSTITUTE OF SCIENCE AND TECHNOLOGY**

# CUSP ENERGETIC PARTICLES: A CASE STUDY FOR PARTICLE TRACING

**M.Sc. Thesis by**

**Altansuvd BOLD**

**511051102**

**Date of submission:** **7 May 2007**

**Date of defense examination:** **11 June 2007**

**Supervisor (Chairman):** **Prof. Dr. Zerefşan KAYMAZ**

**Members of the Examining Committee:** **Assoc. Prof. Dr. Sibel MENTEŞ (İ.T.Ü.)**

**Assist. Prof. Dr. Cuma YARIM (İ.T.Ü.)**

**JUNE 2007**

**İSTANBUL TEKNİK ÜNİVERSİTESİ ★ FEN BİLİMLERİ ENSTİTÜSÜ**

# MANYETİK UÇ BÖLGESİNDEKİ YÜKSEK ENERJİLİ PARÇACIKLAR: PARÇACIK TAKİBİ İÇİN VAKA ÇALIŞMASI

**YÜKSEK LİSANS TEZİ**

**Müh. Altansuvd BOLD**

**511051102**

**Tezin Enstitüye Verildiği Tarih : 7 Mayıs 2007**

**Tezin Savunulduğu Tarih : 11 Haziran 2007**

**Tez Danışmanı : Prof.Dr. Zerefşan KAYMAZ**

**Diğer Jüri Üyeleri: Doç.Dr. Ş. Sibel MENTEŞ (İ.T.Ü.)**

**Yard.Doç.Dr. Cuma YARIM (İ.T.Ü.)**

**HAZİRAN 2007**

**ACKNOWLEDGMENT**

İstanbul Teknik Üniversitesi'ndeki öğrencilik yıllarım boyunca yardımını hiç esirgemeyen Prof. Dr. Zerefşan Kaymaz Hocama teşekkür ederim. Aileme de bana olan desteği için teşekkür ederim.

Bu çalışmada kullanılan modeller NASA'nın CCMC merkezinde çalıştırılmıştır. Modellerin çalıştırılması sırasında karşılaştığımız güçlüklerin giderilmesinde bizlere her zaman anında yardımcı olan CCMC ekibine, özellikle Anna Chulaki'e teşekkür ediyoruz. Bu çalışmadan kendisine ilk bahsettiğimiz andan itibaren yapmamız için bizi sürekli teşvik eden University of California, Berkeley'den Prof. Dr. J.G. Luhmann'a; parçacık takibi kodunun gelişmesi sırasında tecrübelerinden yararlandığımız, University of California, Los Angeles'dan Prof. Dr. R. Richard'a teşekkürlerimizi sunuyoruz.

Bu tez çalışması TÜBİTAK tarafından desteklenmiş olup, TÜBİTAK-104Y039 nolu araştırma projesinin bir parçasıdır.

**Haziran, 2007** **Altansuvd Bold**

**CONTENTS**

## ABBREVIATIONS

| | |
|---|---|
| **CEP** | : Cusp Energetic Particles |
| **IMF** | : Interplanetary Magnetic Field |
| **SW** | : Solar Wind |
| **MeV** | : Mega electron Volt |
| **eV** | : Electron Volt |
| **keV** | : Kilo electron Volt |
| **MeV** | : Mega electron Volt |
| **Open GGCM** | : Open Geospace General Circulation Model |
| **BATS-R-US** | : Block Adaptive Tree Solarwind Roe Upwind Scheme |
| **MHD** | : Magnetohydradynamic |
| **CCMC** | : Community Coordinated Modelling Center |
| **Re** | : Earth radii |
| **nT** | : Nanotesla |
| **nPa** | : Nanop ascal |
| **GSM** | : Geocentric Solar Magnetospheric Coordinates |

**LIST OF TABLES**

**LIST OF FIGURES**

**Page No**

## LIST OF SYMBOLS

| | |
|---|---|
| **a** | **:** Acceleration |
| **v** | **:** Velocity |
| **r** | **:** Position |
| **t** | **:** Time |
| $\Delta t$ , **dt** | **:** Time step |
| **F** | **:** Force |
| **q** | **:** Charge |
| **m** | **:** Mass |
| **E** | **:** Electric field |
| **B** | **:** Magnetic field |
| $\Omega$ | **:** Gyrofrequency |
| $\varepsilon$ | **:** Constant |
| $\gamma$ | **:** Relativistic corrector |
| **c** | **:** Speed of light |
| **u** | **:** Relativistic velocity |
| **x,y,z** | **:** Particle positions |
| $V_x$, $V_y$, $V_z$ | **:** Particle velocities |
| **SW** $V_x$, $V_y$, $V_z$ | **:** Solar wind velocities |
| **IMF** $B_x$, $B_y$, $B_z$ | **:** Interplanetary magnetic field components |
| **R** | : Gas constant |
| **T** | : Temperature |
| **g** | : Gravitational constant |
| $\rho$ | : Mass density |

**CUSP ENERGETIC PARTICLES: A CASE STUDY FOR PARTICLE TRACING**


**SUMMARY**

This study is a first naive attempt to trace the cusp energetic particles backward for the purpose of determining their source. The energetic particles in the cusp region are very controversial topic as to where they come from or how they are produced. The possible sources in the literature may be found as follows:

1. They may be carried along with the solar wind, passed the bow shock and reached the cusp
2. They may be originated within the bow shock with the acceleration of the cold solar wind particles and are carried with the flow through the magnetosheath
3. Shocked solar wind may be subjected to a second acceleration at the magnetopause reconnection region and these particles are carried toward the cusp region
4. They come from the magnetosphere
5. They may be produced and raised to high energies within the cusp region itself.

The discussion of which one is the most widely accepted is beyond the scope of this study. The purpose of this study is first to set up a computer code which is running to trace the particles and integrate the MHD results. Secondly, to adapt and apply the code on a physical problem which in this case tracing the particles in the cusp region. Therefore, in the first part of the thesis, we introduce the characteristics of the cusp region and observations of energetic particles and present the findings in the literature.

In Chapter 2, Interball observations were used. Two examples of cusp crossings were selected and CCMC/NASA models (Community Coordinated Modelling Center) were run for these events. The cusp observations were described using these events and the features in the cusp were compared with those obtained from the CCMC models. Here, also the CCMC utility at NASA to run the space weather models, BATS R US and open GGCM (General Global Circulation Model) that were

used for the comparisons were introduced. The corresponding IMF and solar wind plasma dependence of the cusp features are also discussed through the comparisons. The purpose in this chapter is to show the weaknesses and strengths of the models; determine where and when it fails or it is successful to represent the observations.

In Chapter 3, a particle tracing code was developed. First literature search on this was given and the method was used to trace the particles. The code was tested with the theoretical expectations and also using the MHD model results. MHD model results in the code are used to push the particles from their positions. Here are the particle trajectories for northward and southward IMF cases presented and the differences are discussed.

In Chapter 4, the results are summarized and the study was concluded with some suggestions for future work.

Especially the particle tracing code developed in this study is still under improvement. To test the code with more real cases before moving on to address real physical problems will be the next step. MHD model comparisons also will be continued with more event studies to draw statistical conclusions.

**MANYETİK UÇ BÖLGESİNDEKİ YÜKSEK ENERJİLİ PARÇACIKLAR: PARÇACIK TAKİBİ İÇİN VAKA ÇALIŞMASI**

## ÖZET


Bu çalışma, manyetosferin kutupsal uç bölgesinde (cusp) görülen yüksek enerjili parçacıkların geriye doğru takibi ile bu parçacıkların kaynaklarına ait bilgi edinmek konusunda ilk defa yapılan, uydu gözlemlerine dayalı çalışmadır. Cusp bölgesindeki yüksek enerjili parçacıkların nereden geldikleri ve nasıl oluştukları çok tartışmalı bir konudur. Literatürde bu parçacıkların nereden kaynaklandığına dair şunlar bilinmektedir:

1. Yüksek enerjili parçacıklar Güneş'te üretilip güneş rüzgarı ile birlikte Dünya'nın yay şoku bölgesini geçerek cusp bölgesine ulaşırlar
2. Yüksek enerjili parçacıklar daha soğuk olan güneş rüzgarı parçacıklarının Dünya'nın yay şoku bölgesinde hızlandırılmalarını takiben enerjilerinin artması sonucunda oluşurlar
3. Yüksek enerjili parçacıklar manyetopoz bölgesinde oluşan manyetik birleşme sonucunda oluşurlar ve cusp bölgesine taşınırlar
4. Manyetosferde oluşturulurlar ve cusp bölgesine taşınırlar
5. Cusp bölgesinde lokal işlemler sonucunda oluşurlar

Bu kaynaklardan hangisinin kabul gördüğü ve neden kabul gördüğü tartışmaları, bu çalışmanın konusu dışındadır. Bu çalışmanın ana amacı, MHD model sonuçlarını girdi olarak kullanan ve parçacıkları takip eden bir bilgisayar kodunu oluşturmaktır. Kodun test edilmesi tamamlandıktan sonra, onu fiziksel bir problemin çözümünde, ki bu çalışmada cusp bölgesinin enerjetik parçacıklarının takibidir, kullanmaktır. Bu nedenle tezin ilk bölümünde, cusp bölgesinin, yapısı, karateristik özellikleri ve bu bölgede görülen enejetik parçacıklar hakkında ön bilgi verilmiştir.

İkinci bölümün ilk kısmında gözlemsel çalışmalarımızın sonuçları sunulmuştur. Çalışmamızda NASA/CDAWEB sayfasında herkese açık, Interball uydusu verileri kullanılmıştır. Enerjetik parçacıkların görüldüğü iki "vaka"ı örnek seçerek bu parçacıkların görüldüğü IMF ve güneş rüzgarı şartlarını incelenmiştir. İkinci bölümğn ikinci kısmında ise once CCMC/NASA Space Weather modelleri (BATS R US ve

açık GGCM (General Global Circulation Model) hakkında bilgi verilmiş, daha sonra gözlem sonuçları model sonuçları ile karşılaştırılmıştır. Bu kısımda amaç, cusp örneği için çalıştırılan bu Space Weather modellerinin gözlemleri ne kadar iyi yansıttığı, veya en çok farklılık görüldüğü noktaları belirlemektir. IMF ve güneş rüzgarına bağımlılık model sonuçları ile ortaya konulacaktır.

Bölüm 3'de parçacık takibi için literatür araştırması verilmekte ve Parçacık Takip Kodu'nun geliştirilmesinde kullandığımız metod anlatılmakta ve kodun sonuçları teoriden beklenen sonuçlarla test edilmektedir. İki reel vaka örneği için parçacık kodunun sonuçları verilmektedir. CCMC model sonuçları parçacık kodunda parçacığı ilerletmek için kullanılmaktadır. Alınan ilk onuçlar iki farklı IMF, kuzeyli ve güneyli, için tartışılmaktadır.

Bölüm 4'de elde ettiğimiz sonuçları özetlemekte ve gelecek çalışmalar için önerilerde bulunmaktayız.

Burada sunduğumuz parçacık kodu ve MHD model karşılaştırmaları vaka sayısı artırılarak devam etmektedir. Parçacık kodu bir çok vaka için test edildikten sonra reel bir fiziksel problemin çözümünde kullanılabilir hale gelebilecektir.

# 1. INTRODUCTION

The polar cusp is an essential part of the Earth's dayside magnetosphere. When the earth dipole magnetic field is enclosed by the magnetopause current sheet, two zero points or neutral points, that has near zero magnetic field, one in each hemisphere are formed. Dayside magnetosphere's magnetic field lines and those of tail lobes curve down around these neutral points. These curvatures of magnetic field lines form a funnel like structure as shown in Figure 1.1. This funnel maps down near to noon auroral oval at the ionosphere.

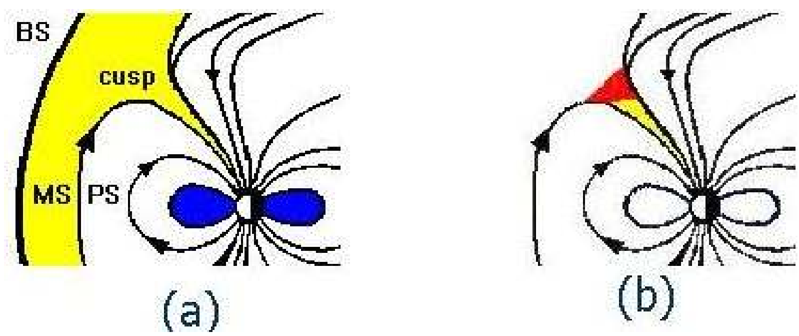


**Figure 1.1:** (a) Bow Shock (BS), Magnetosheath (MS) and cusp region. (b) The cusp funnel is the yellow region and red region is the exterior cusp.

This funnel is called cusp and exterior cusp is its upper region. The exterior cusp connects directly to the magnetosheath. The exterior cusp is defined as the region next to magnetopause with observable decrease in magnetic field strengths, and usually around 2-3 Earth Radii (Re) radial distance of the topological minimum B point (Sheldon et al, 1998). Russell (2000) defined the exterior cusp as a region, in which magnetic field strength fall, located outside the magnetopause. Through the cusp funnel solar wind particles can enter ionosphere and also ionospheric ions can flow out to the magnetosphere. The exterior cusp is also called the high-altitude cusp. The low-altitude cusp can be defined as follows [1]:

"The low-altitude cusp is the dayside region in which the entry of magnetosheath plasma to low altitudes is most direct. Entry into a region is considered more direct if more particles make it in (the number flux is higher) and if such particles maintain more of their original energy spectral characteristics".

The location of the cusp depends on several factors. Among those are the shape of the magnetopause, direction of Interplanetary Magnetic Field (IMF), solar dynamic pressure, geodipole tilt angle, distribution of magnetospheric plasma and the rate of reconnection. Measurements have shown, that the cusp is highly confined region, extending about 2.5 hours in local time. However, because of the strong dependence of the cusp position on IMF conditions, the statistical studies show somewhat larger cusp regions. For an intermediate magnetopause shape, the invariant latitude of the cusp changes between 77-90$^o$.

Figure 1.2 shows the cusp's location dependence on the magnetopause shape in a non-reconnecting magnetosphere. These are (a) planar magnetosphere, (b) spherical magnetosphere, (c) elliptical magnetosphere, (d) empirical magnetosphere. In the planar model of Chapman Ferraro magnetosphere in 1930, the cusp is seen as the point where the magnetic field lines diverge. This occurs at 77$^o$ invariant latitude, i.e. the latitude at which the magnetic field line intersects the surface of the Earth. In the spherical model, it is seen directly over the pole on the geodipole axis. In panel d, the cusp position is shown using the empirical model of Tsyganenko (1989a) which gives 78$^o$ invariant latitude. The location of cusp as seen from panel d, also depends on the magnetospheric plasma distribution as taken into account in the empirical model (Russell, 2000).

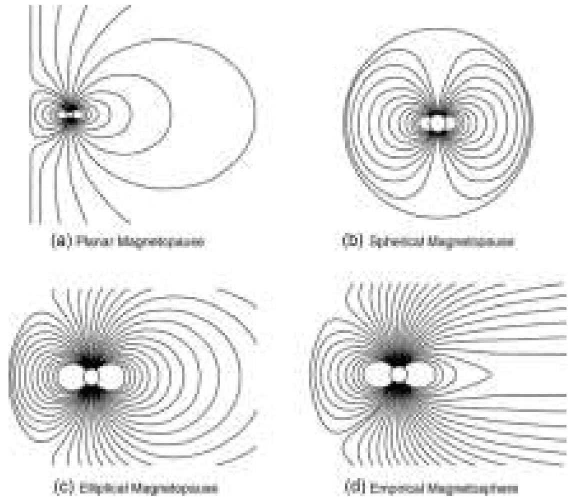

**Figure 1.2:** Dependence of the polar cusp location on the shape of the magnetopause: (a) in planar magnetosphere, (b) in spherical magnetosphere, (c) elliptical magnetosphere, (d) empirical magnetosphere of Tsyganenko (1989b) (Russell, 2000).

In a reconnecting magnetosphere, the location of cusp is either seen equatorward of the reconnection point which happens when IMF is northward, or poleward of the reconnection point which happens when IMF is southward. In these two IMF orientations, the configuration of the magnetospheric field lines is different owing to the reconnection. Figure 1.3 gives the expected configuration of magnetospheric field lines for southward and northward IMFs (Dungey, 1961). The reconnection takes place at different locations for these two cases; at the subsolar location for southward IMF and at the poles for northward IMF. The magnetospheric plasma processes which operate differently for these two cases affect the location of the polar cusp observed (Russell, 2000).

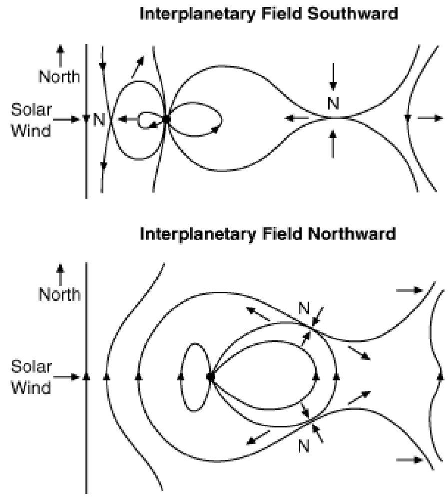


**Figure 1.3:** Reconnecting magnetosphere for southward (upper) and northward (lower) IMF and relation to polar cusp (Dungey, 1961).

Figure 1.4 shows the dependence of the polar cusp location on the IMF Bz using Polar observations. In the figure, the cusp center is seen to be at $81.3^{o} \pm 0.98Bz$ invariant latitude for southward IMF, where Bz is nT and negative for southward fields, while for northward IMF, it is found to be at $80.7 \pm 0.027$ Bz. With increasing northward component of IMF, it is seen that the cusp location moves to equatorward (Russell, 2000) and also is wider in invariant latitude (Zhou et al, 2000). The decreasing cusp latitude with increasing northward IMF can be understood in terms of the cusp reconnection taking place with the northern latitude field lines of the magnetosphere (Russell, 2000).

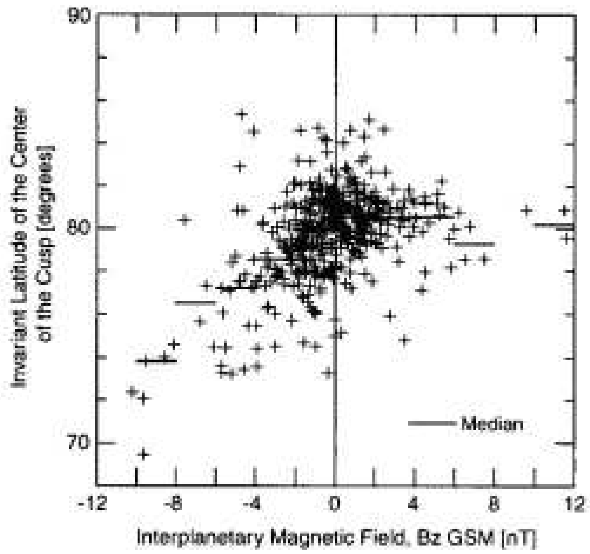


**Figure 1.4**: Polar observations of cusp location and its dependence on IMF (Zhou et al. 1999, Russell, 2000).

Similarly, Newell et. al. (1989) looked at the location of the equatorward boundary of the cusp with IMF Bz and their result is given in Figure 1.5. It is seen that their fit to DMSP polar cusp observations is $77 \pm 0.7$Bz for southward IMF and $77.2 \pm 0.11$Bz for northward IMF.

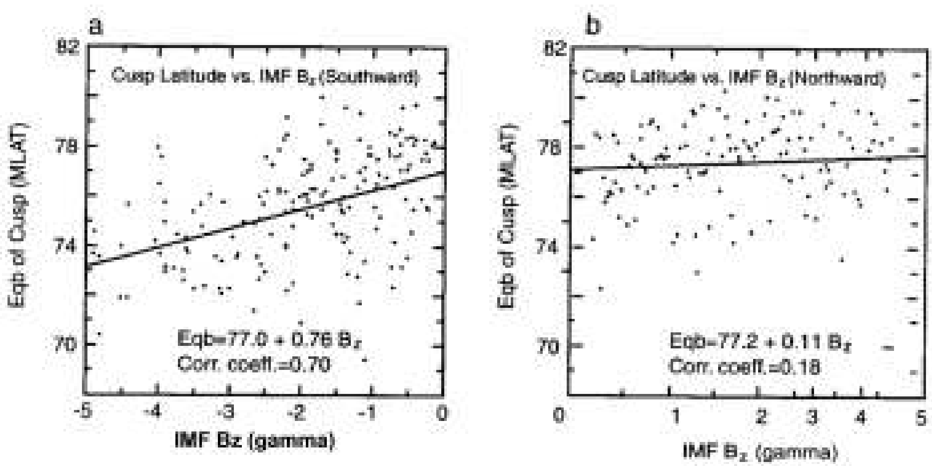


**Figure 1.5**: DMSP observations of polar cusp equatorward boundary dependence on IMF Bz (Newell and Meng, 1989).

Zhou et al. (1999) also investigated the dependence of the cusp location on the IMF By component. Figure 1.6. sketches IMF By influence on the cusp position.

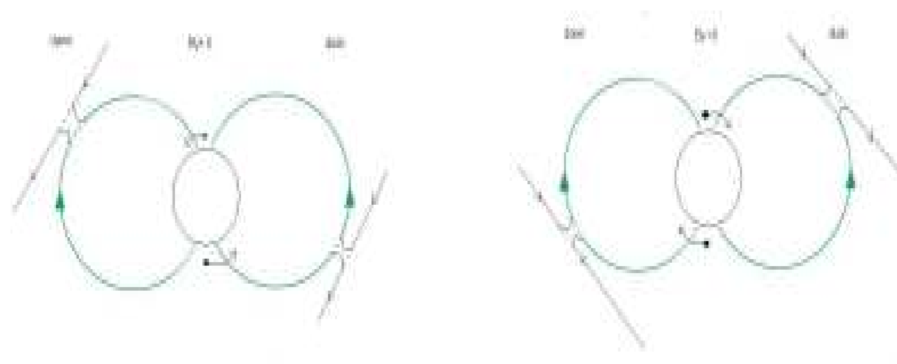

**Figure 1.6:** Influence of IMF $B_y$<0 and IMF $B_y$ >0 on the cusp position through magnetic reconnection

Especially during southward IMF a positive By component shifts the northern cusp duskward and negative By dawnward. Zhou et al. (1999) found that for IMF By>6nT, the cusp is displaced about 1 hour in local time toward afternoon side and for IMF By <-6nT it is displaced about 2 hours toward morning.

Fritz and Zong (2004) investigated the dependence of the width of the polar cusp on the IMF and found that the cusp latitudinal width increases with IMF Bz, and the equatorward boundary moves to lower latitude with increasing IMF By (Fritz and Zong, 2004). On the other hand, IMF Bx is found to have no effect on cusp position. In addition to the direction of IMF, the history of IMF also affects the cusp location. Simunek et al. (2003) suggested that the cusp does not change instantaneously with changes in IMF but is responsive to the history of IMF. He showed that the reconfiguration of the cusp due to an IMF change can take approximately 15 minutes.

The effect of the solar wind dynamic pressure on the cusp position as well is investigated by Zhou et al. (1999) using Polar observations as the magnetopause move in and out as the dynamic pressure increases and decreases. They found that the cusp thicker and wider in local time during the high solar wind dynamic pressures. Figure 1.7 illustrates these findings.

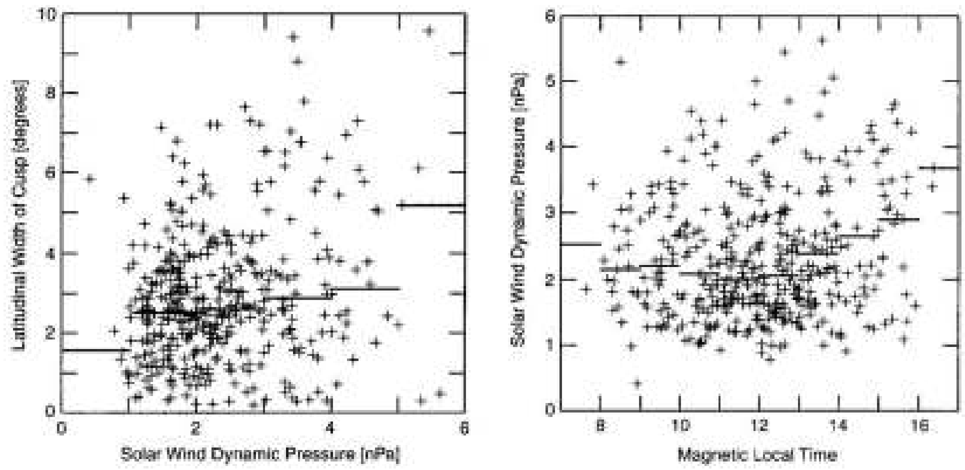


**Figure 1.7:** Dependence of cusp latitudinal width (left) and location in magnetic local time (right) on dynamic pressure (left) using Polar observations (Zhou et al., 1999).

The geodipole tilt, the angle between the Earth's north dipole axis and geocentric solar magnetospheric coordinates (GSM) z-axis, is another factor that affects the position of cusp. Zhou et al. (1999) showed that the cusp location changes about 5$^{o}$ for a tilt change of 70$^{o}$ or about 1$^{o}$ invariant latitude for every 14$^{o}$ of tilt. Figure 1.7 shows the locations of the cusp detected by POLAR during northward IMFs for three tilt angle ranges 0-10$^{o}$ , 10-20$^{o}$ and =20$^{o}$ respectively. The magnetic field lines drawn are those from the Tsyganenko 1989 vacuum magnetosphere for tilt angles of 5$^{o}$, 15$^{o}$ and 25$^{o}$. These three figures that the invariant latitude of the cusp varies with the tilt angle of the dipole both in the data and in the model. The amount of shift with tilt observed is consistent with that expected from the model. Using DMSP spacecraft, Newell and Meng (1989) showed the change in the location of the equatorward of the cusp boundary as a function of tilt angle. Their result is that the cusp varies by 4$^{o}$ over a tilt change of 60$^{o}$ for all IMFs. At 20$^{o}$ tilt, this is consistent with the 2$^{o}$ change observed by POLAR. Figure 1.8 and Figure 1.9 give results of the tilt dependence of the cusp location from Polar observations and DMSP spacecraft.

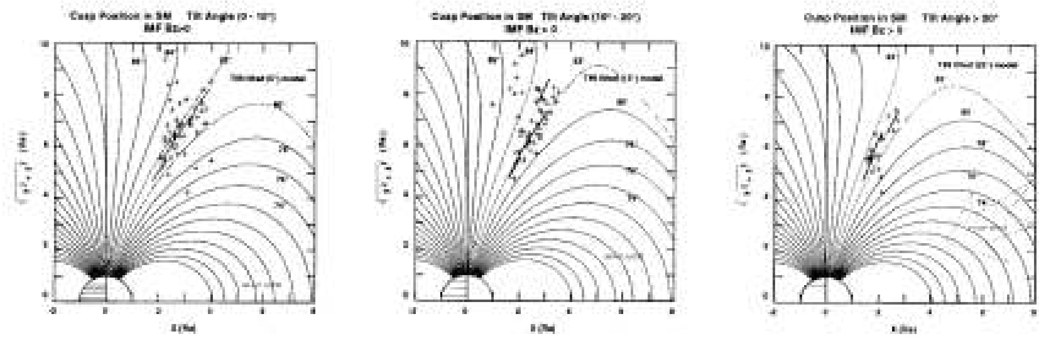

**Figure 1.8**: Polar observations of cusp location and its dependence on tilt angle (Zhou et al. 1999, Russell, 2000). IMF is northward during the events.

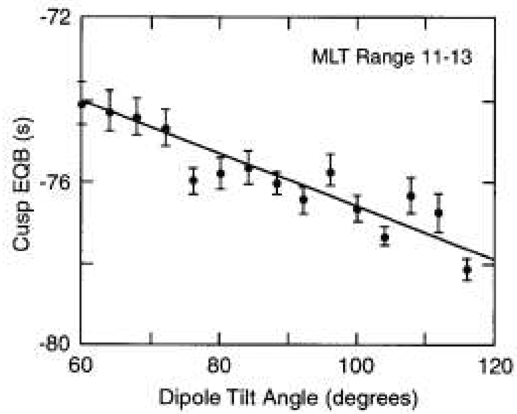


**Figure 1.9**: DMSP observations of polar cusp equatorward boundary dependence on tilt angle for all IMF (Newell and Meng, 1989).

### 1.1. CUSP IDENTIFICATION

For a long time since their launch, HEOS (Harendel et al, 1978) and Hawkeye (Farrell and Van Allen, 1990) observations were the only spacecraft that provided information about cusp and its surrounding regions. At high altitudes, OGO-5, IMP-5, and at lower altitudes DMSP satellites provided data to drive the main characteristics of cusp that are available in most of the literature today.

With the launch of POLAR spacecraft in 1996, high resolution data have become available to analyze. In the observations, the cusp region is recognized by looking at the ion and electron density, velocity, composition, magnetic fields, and presence of energetic particles. Figure 1.10 gives an example where the cusp has seen in Polar observations by Zhou et al. (1999).

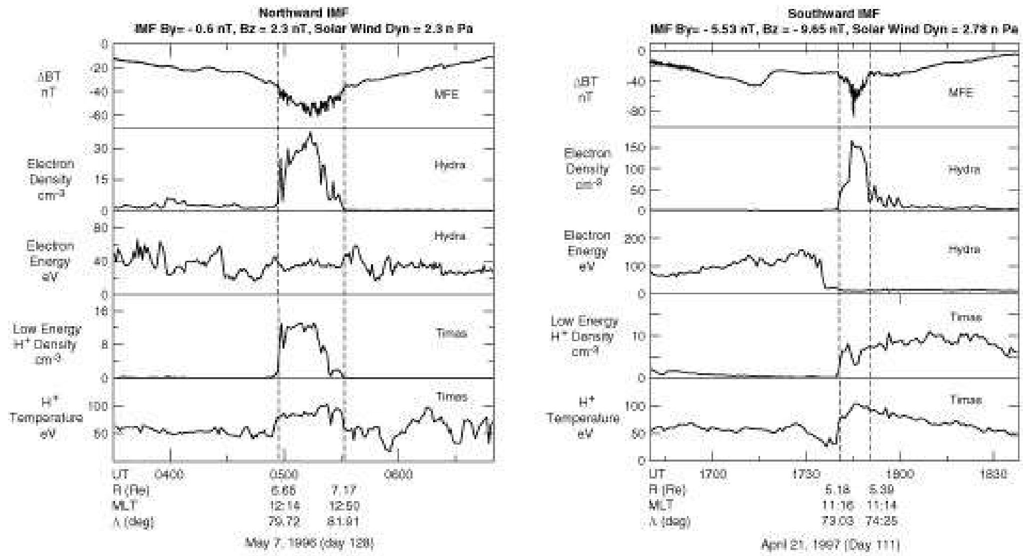


**Figure 1.10**: Polar spacecraft cusp observations for northward (left) and southward (right) IMF. Panels from top to below are magnetic field, electron density, electron energy, $He^+$ density and temperature (Zhou et al., 1999).

As seen in Figure 1.10, the magnetic field in the cusp region is depressed and become fluctuated. The decrease in magnetic field pressure due to a decrease in the magnetic field strength is compensated by an increase in thermal pressure of the cusp plasma.

Figure 1.11 was taken from Pissarenko et al. (2001) and shows two cases of the cusp crossings of INTERBALL spacecraft. Interball observations are used as they are readily available on CDAWEB site [2] except the energetic particle spectral data. Since MHD model results were compared with Pissarenko et al.'s case of cusp observations in Chapter 2, here only how the energetic particles relate to the cusp and its regions are described.

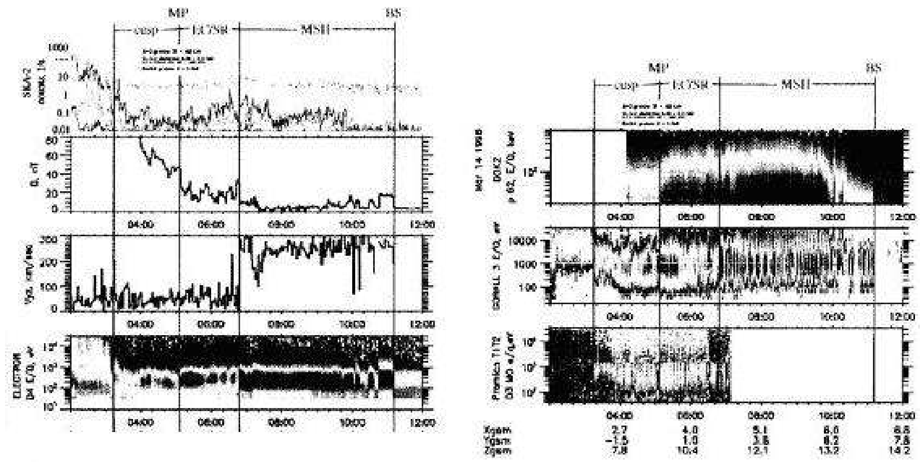


**Figure 1.11**: Interball observations of cusp on 14th of March 1996 and 21st of April 1996. The panels from top to bottom give high energy particle fluxes, total magnetic field, E-T spectrograms from ELECTRON and DOK-2.

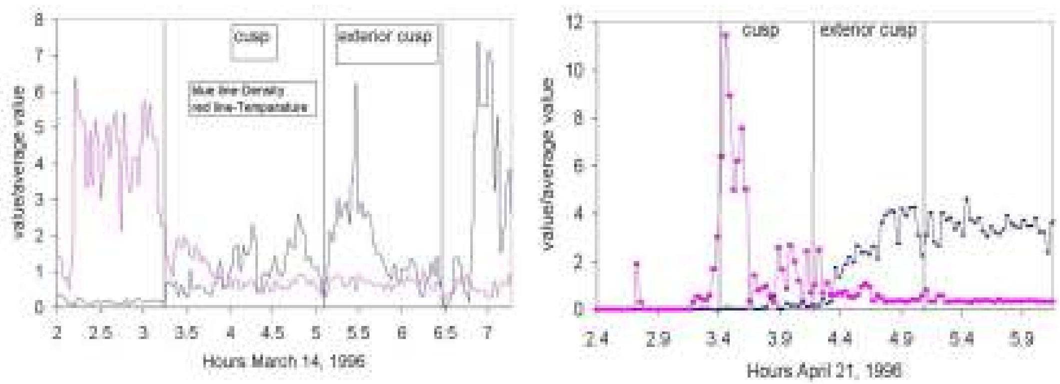


**Figure 1.12**: Interball observations of cusp on 14th of March 1996 and 21st of April 1996. The panels include CORALL density and (blue) and temperature (red). The data were normalized to the average within the crossing interval.

Using Figure 1.11 and Figure 1.12, the cusp region was recognized from surrounding regions with:

1. a decrease in magnetic field compared to magnetospheric fields
2. a increase in the ion number density when the spacecraft is coming from magnetosphere
3. a decrease in temperature compared to surrounding magnetosheath and magnetospheric regions
4. the presence of high energetic particles

Using these signatures, Pissarenko et al. (2001) defined cusp from 03:00 to 05:04 UT and in the second event studied in Chapter 2.1, from 03:24 to 04:12 UT.

Recently, using POLAR observations, Chen et al. (1998) observed high energetic particles within the cusp on the order of Mega Electron Volts (MeVs) and they have described these events as CEP (Cusp Energetic Particles). Findings about these CEP events are (Chen and Fritz, 1999):

- They were detected on the dayside cusp.
- Large fluxes of energetic (>20 keV) ions were observed for periods of hours where such quasi-trapped ions should not be stably trapped.
- The associated magnetic field is turbulent and greatly depressed appearing to reach a null value in many cases.
- The 1-200 keV/e helium ions are $He^{++}$
- Compared to $O^{>+2}$, the $O^{<+3}$ is negligible.
- At 1-200 keV/e, the $He^{++}$ particles are the dominant heavy ions with an intensity of about one order of magnitude larger than the oxygen ions.

In Figure 1.13, the features of the CEP events observed in August 27, 1996 are shown. Figure 1.14 gives positions of 35 CEP events determined in 1996 from POLAR spacecraft.

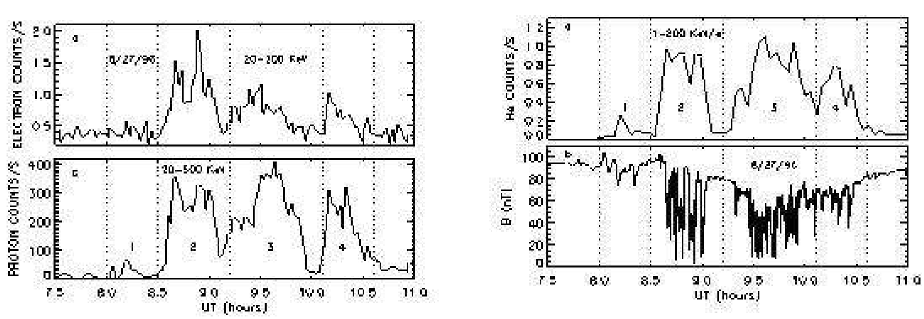


**Figure 1.13:** Magnetic field, proton, electron and helium count rates for August 21, 1996 CEP. The vertical dash lines mark the 4 different regions in the events (Chen, 1998).

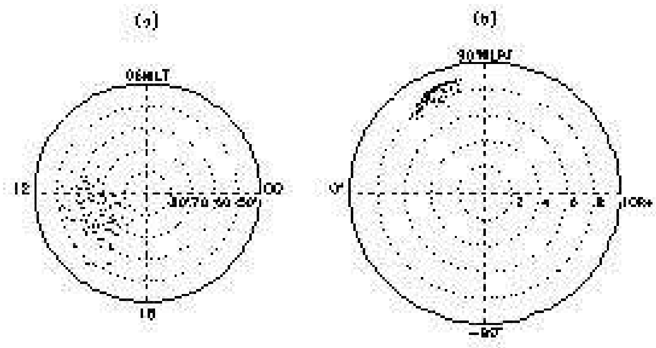

**Figure 1.14:** The event averaged positions of the CEP events in the magnetosphere with a) MLT versus MLAT, the four dashed circles from inside to outside indicate the MLAT positions from 80$^{o}$ to 50$^{o}$ b) MLAT versus R in polar coordinate, and the dashed circles represent the distance of Polar from the Earth in Re (Chen, 1998).

### 1.2. ENTRY OF PARTICLES THROUGH CUSP

Polar cusps provide a direct entry for the magnetosheath plasma into the magnetosphere. The magnetosheath plasma penetrating into the low-altitude cusp is responsible, for example, for part of the dayside auroral precipitation. Recent measurements by the Polar satellite have shown that also ions in the MeV range are present (Chen et al., 1998), called as CEP events. In addition to plasma, many types of waves and turbulent flows also access to the ionosphere via the cusp. These are:

- solar wind variations
    - including those generated in the foreshock upstream of the bow shock
- radiation from the parallel and perpendicular shocks
- magnetosheath turbulence and waves
- magnetopause boundary variations due to, e.g.,
    - flux-transfer events
    - pressure variations
    - Kelvin-Helmholtz instability
- waves and particle variations which take place in the boundary layers just inside the magnetopause.

The low-altitude cusp is the focus of these phenomena and ground observations are comprised of their superposition. Also, the flow near the cusp is like a hydrodynamic flow around a corner, in which vortex formation and separation are known to occur and to initiate some level turbulence. Because of these features, cusp is the region of turbulent magnetic fields with shocked solar wind plasma and occasionally with plasma of ionospheric origin.

### 1.3. ENERGETIC PARTICLES AND CUSP

One of the key features of cusp region that distinguish it from the surrounding magnetospheric regions is the presence of the energetic particles. The source of the energetic particles has always been and still is a controversial issue. The possible sources for cusp energetic particles can be identified as follows:

1. Solar Wind: energetic solar wind particles may be carried through bow shock to magnetosheath and to the cusps.
2. Accelerated particles may come from the bow shock (Chang et al., 1998).
3. They may come from the magnetosphere with several mechanisms suggested (Antonova et al., 2000).
4. They may be produced within the cusp locally (Chen et al., 1998).

Ions with magnetosheath energies (typically ~1-2 [keV/e]) in the Earth's magnetospheric cusps are suggested to originate in the solar wind (Fuselier et al, 2002). It is shown that these particles enter the cusp through reconnection. Reconnection can take place when the IMF is both southward and northward. The statistical properties of cusp or the individual case events are found consistent with the cusp entry through reconnection (Onsager et al., 1995).

At energies higher than those of magnetosheath, there is a debate over the origin of the ions in the cusp. Chen et al. (1998) observed two different group of particles with energies ≤ 150 [keV/e] and greater than 150 [keV/e]. The particles at lower energies from 10 [keV/e] to 150 [keV/e] are suggested to originate from the quasi parallel shock (Chang et al., 1998; Tratttner, et al., 2001). For the origin of the higher component particles above 150 [keV/e], two sources of origin are proposed. One is the dusk side magnetosphere, and in the end the plasma sheet and the other is the cusp itself. While the local acceleration of particles within the cusp is not well investigated as it requires an unknown acceleration mechanism which operates within the cusp, the magnetospheric origins are supported by the statistical data (Karra and Fritz, 1999). On the other hand, Antonova et al. (2002) suggests nightside acceleration mechanisms associated with the substorm activity and subsequent transport into cusp region rather than a local acceleration as opposed to Chen et al.'s (1998) local cusp acceleration.

## 2. INTERBALL CUSP EVENTS AND MODEL COMPARISONS

In this section, the CCMC model results will be compared with the cusp observations identified in Interball observations. First, the Interball cusp events are described and then the model and the model results are explained.

### 2.1. INTERBALL CUSP EVENTS

Interball spacecraft with its polar elliptical orbit gives a good opportunity to study the high latitude magnetosphere and cusp region. In this study, as the energy time spectrums of energetic particles were not available to us, two cusp transitions which were already defined by Pissarenko et al. (2001) were selected and described partially in Chapter 1 of this thesis. Two events are observed in March 14, 1996 and April 21, 1996. Thereafter, these will be called as Event 1 and Event 2.

Figure 2.1 shows the INTERBALL orbits for the selected 2 events in xz- and xR-planes. The cusp, as defined by Pissarenko et. al. (2001) in accordance with the cusp signatures defined in Chapter 1.2, was observed from 03:08 to 05:04 UTM during Event 1 and from 03:24 to 04:12 UTM during Event 2. The data from ASPI MIF-M/ PRAM, SKA-2, DOK-2, CORALL and VDP instruments are used. ASPI MIF-M/ PRAM magnetometer instruments measure magnetic fields; CORALL instruments measure Ion moments which then Ion Number Density, Ion temperature, Ion velocity in GSE and GSM Cartesian vector, Ion velocity, vector magnitude are calculated; DOK2 and SKA 2 instruments measure electron and proton flux and VDP instruments measure total antisunward ion flux. All Interball data are provided in 2 min resolution on CDAWEB/NASA web page.

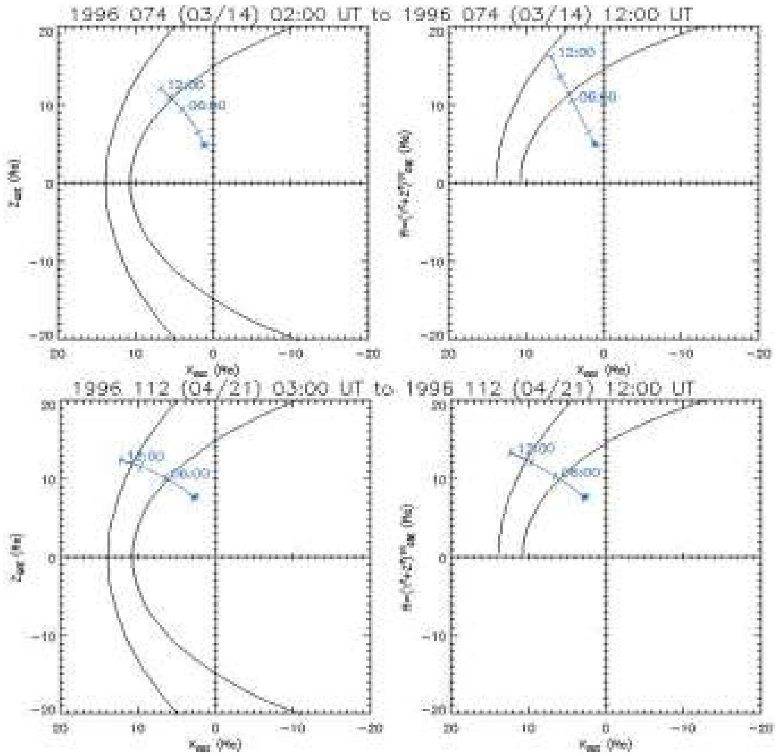


**Figure 2.1**: Interball trajectory through the cusps in xz- an xR-plane for both Event 1 (top) and Event 2 (bottom) used in this study.

Figure 2.2 gives the density and density temperature variation with time as the spacecraft moves from magnetosphere into the solar wind for Event 1. The magnetic field variation is presented in the top panel of energetic particle figure in Figure 1.11. The regions traveled by the spacecraft during the events are shown in vertical lines using Pissarenko et al.'s identification (2001). The vertical axis shows the ratio of density and temperature data to their proper average value within the crossing. In Figure 2.2, as the spacecraft enters the cusp at 03:08 UT, ion number density increased (blue line in figure), and ion temperature (red line) decreased. The invariant latitude of the cusp corresponds to 54.65$^o$-56.81$^o$. Magnetopause according to Pissarenko et al. (2001) is observed at 05:04 UT. Exterior cusp is seen from 05:04 to 06:27 UT. Invariant latitude for the exterior cusp was seen between 56.81$^o$-56.73$^o$. From the Figure 2.2, it can be seen that magnetic field in cusp is higher than that of the exterior cusp region. The tilt angle in this period changed from -12.2$^o$ in xz-plane and 31$^o$ in yz-plane.

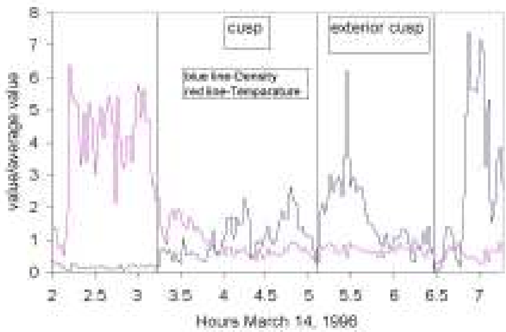


**Figure 2.2:** INTERBALL density and temperature data during the crossing of cusp observed on 14 March 1996

Observed energetic particles from (Pissarenko et al., 2001) for this event are given in Figure 1.11 in Chapter 1. Pissarenko et al. (2001) use this data to identify exterior cusp and cusp region. The presence of energetic ions are present though the magnetosheath. However, it is in the cusp that level of energy is slightly higher in the cusp and exterior cusp and it is more fluctuated in the cusp than in the exterior cusp.

Figure 2.3 gives the IMF Bz and solar wind dynamic pressure conditions during the spacecraft crossing of Event 1. The IMF measured by WIND was shifted to account for the solar wind convection time. As can be seen from figure, the $B_z$ component of IMF was southward and the $B_y$ component was changing its sign from negative to positive during the cusp crossing. The average IMF Bz corresponding to cusp interval is -2.5 nT and the dynamic pressure of the solar wind (right panel in Figure 2.3) corresponding to the cusp interval is about 1.5 nPa on the average.

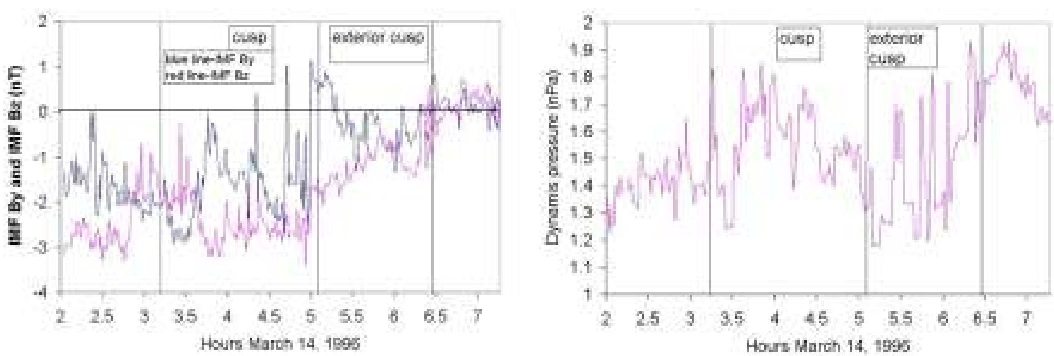


**Figure 2.3:** IMF Bz and By (left) and solar wind dynamic pressure (right) during Event 1 from WIND spacecraft.

Figure 2.4 overlays the wind density data with the Interball density to compare the features between the cusp and the solar wind. It was seen that  that the densities do not change in the solar wind and stay at about 3 #/cc during cusp crossing while the density in the cusp shows high variability.

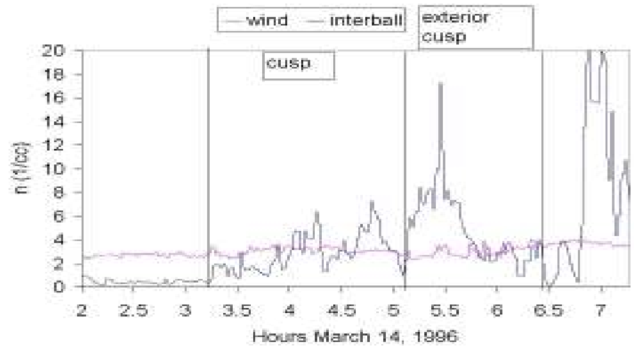


**Figure 2.4:** Plasma data (plotted is density) measured by WIND and INTERBALL during Event 1

Event 2 by INTERBALL-Tail Probe was observed cusp on 21st April 1996 (Pissarenko et al., 2001). The trajectory of the spacecraft for this event is seen at the bottom panels in Figure 2.1. Figure 2.5 presents the density and temperature variations while the spacecraft crosses through from the magnetosphere out to the solar wind.

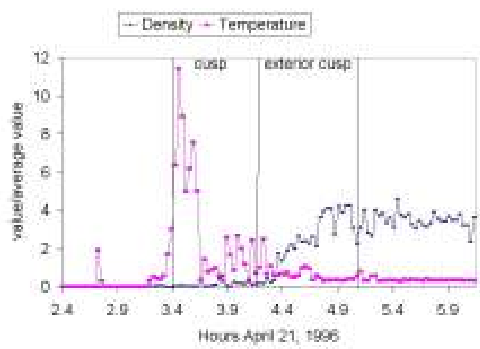


**Figure 2.5:** INTERBALL crossing of cusp and exterior cusp on 21 April 1996

The data in Figure 2.5 together with energetic particle data given below in Figure 2.6 showed that the spacecraft crossed the cusp between 03:24 and 04:12 UT.

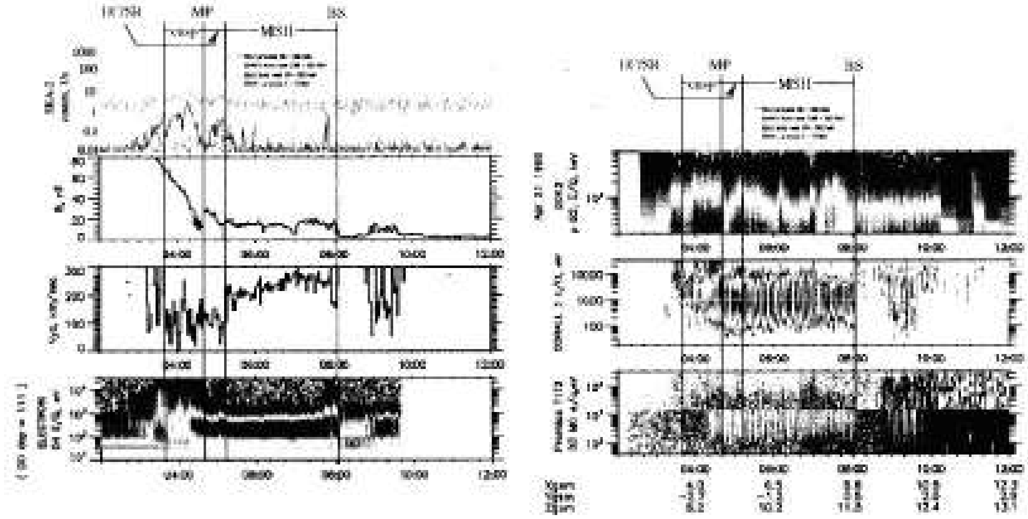

**Figure 2.6**: Interball observations of cusp on the day of 21st of April 1996. The panels from top to bottom give high energy particle fluxes, total magnetic field, E-T spectrograms from ELECTRON and DOK-2.

In Event 2, as spacecraft entered the cusp from the magnetosphere, while the ion number density decreased, ion temperature is seen to increase in Figure 2.6. Also the energetic particles are detected. As seen in Figure 2.6, the fluctuating high energy part of the energetic particles is obvious within the cusp while exterior cusp and the magnetosheath present much smoother structure of the energetic particles. The tilt angle during this crossing is 3.9$^o$ in xz plane and 27.6$^o$ in yz plane.

Figure 2.7 shows the IMF Bz and solar wind dynamic pressure conditions during the spacecraft crossing of Event 2. As in Event 1, the IMF and solar wind data were shifted to account for the solar wind convection time. As can be seen from the figure, the $B_z$ component of IMF was northward during spacecraft's cusp encounter and the $B_y$ component was negative. Corresponding cusp invariant latitudes for this event is between invariant latitudes 60.47$^o$-60.5$^o$. Exterior cusp was seen between 60.5$^o$-59.82$^o$.

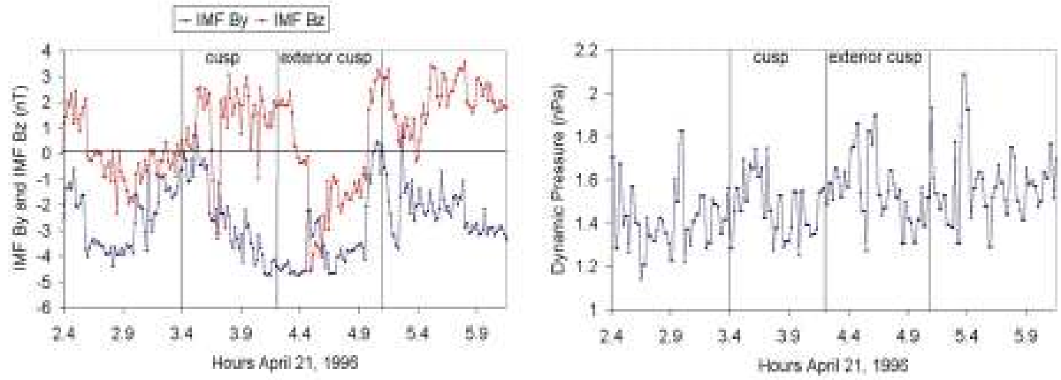


**Figure 2.7:** IMF Bz and By (left) and solar wind dynamic pressure (right) during Event2

Figure 2.8 gives the overlaid image of solar wind density with Interball density for Event 2. The solar wind density is seen to be constant at 3 #/cc. It is a low density solar wind. The density in the cusp for Event 2 is lower than the density observed in Event 1.

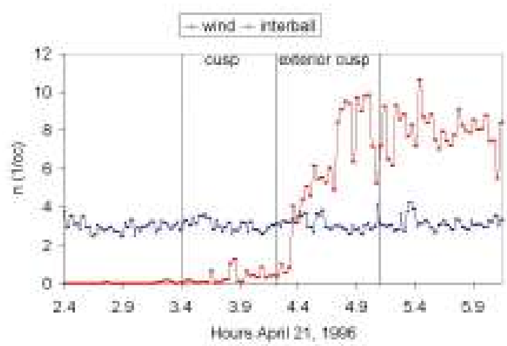


**Figure 2.8:** Plasma parameters measured by WIND and INTERBALL during Event1

## 2.2. MHD MODEL SIMULATION

### 2.2.1. CCMC Models

The Earth's magnetosphere is a very dynamical system. It’s the result of interaction between internal and external factors. Internal factor is the Earth's magnetic axis orientation with respect to the Sun-Earth line. This orientation varies with time because of both the Earth's diurnal rotation and its motion around the Sun. External factor that forces magnetosphere is the state of the solar wind. To understand the magnetosphere, the structure of geomagnetic field and it’s the relation with the solar wind must be known. Schematic of some magnetospheric regions can be seen in Figure 2.9. Space scientists are trying to develop high-resolution simulation models of the magnetosphere and solar wind interaction, in order to be able to compare spacecraft measurements with these models to determine the underlying physics that controls the magnetospheric dynamics.

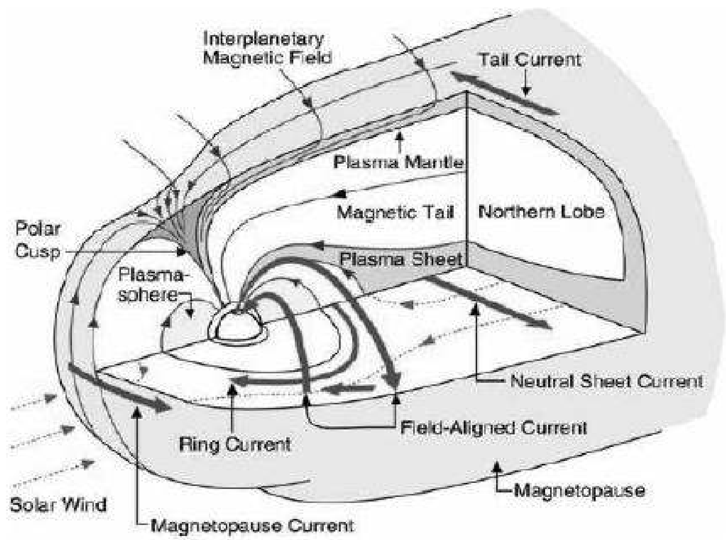


**Figure 2.9:** Schematic view of magnetosphere and its dynamics

Space Weather Models or Magnetohydrodynamic (MHD) global simulation models are three-dimensional numerical solution of the ideal MHD equations which are the basic equations for mass, momentum, energy and magnetic flux.

$$\frac{\partial \rho}{\partial t} + \nabla \bullet (\rho \mathrm{v}) = 0 \quad (2.1)$$

$$\frac{\partial p}{\partial t} + \mathrm{v} \bullet \nabla \mathrm{p} = -\gamma \mathrm{p} \nabla \bullet \mathrm{v} \quad (2.2)$$

$$\rho \frac{\partial \mathrm{v}}{\partial t} + \rho (\mathrm{v} \bullet \nabla) \mathrm{v} = -\nabla \mathrm{p} + \mathrm{j} \times \mathrm{B} + \rho \mathrm{g} \quad (2.3)$$

$$P = 2 \rho R T \quad (2.4)$$

$$j = \frac{\nabla \times B}{\mu} \quad (2.5)$$

$$\nabla \cdot B = 0 \tag{2.6}$$

$$\frac{\partial B}{\partial t} = -\nabla \times E \tag{2.7}$$

$$\frac{j}{\sigma} = E + \mathrm{v} \times B \tag{2.8}$$

It is realistic because plasma is in interaction with the magnetic field. Global modeling of the magnetosphere-ionosphere system began about 20 years ago with the first simple MHD models of the solar wind - magnetosphere interaction. The first models were two-dimensional, next three-dimensional models were developed. Then the electrodynamics of ionosphere and the connection between magnetospheric and ionospheric convection were included. The model results have been found to be consistent with in-situ measurements (Raeder, 2003).

MHD is the only physical approximation that can be used for time dependent three-dimensional global modeling because of the limitations in computer resources. The MHD models are self-consistent, time-dependent models of the solar wind-magnetosphere-ionosphere system. MHD models place a spherical shell with a radius of 3 to 4 around the earth, to exclude the region where the Alfven velocity becomes too large to be computed in the simulation. Inside the shell MHD equations are not solved and a static dipole field is assumed (Fuselier et al., 2002). These MHD models have been successful in predicting the expected solar wind and magnetosphere interaction result.

The ability to simulate and predict space weather phenomena is important for many areas such as the success of spacecraft missions and the reliability of satellite communication equipment. In extreme cases magnetic storms have effects on power grids used by households (Toth et al., 2005). Therefore, the prediction of the solar activity and its Earth’s arrival become very important for technological limits on Earth and space based systems. MHD models, thus, take a crucial role in the prediction of the phenomena and its end interaction with the Earth’s magnetic environment.

### 2.2.2. BATS-R-US

Block Adaptive Tree Solar Wind Roe Upwind Scheme (BATS-R-US) was developed at the University of Michigan. BATS-R-US uses arranged rectangular blocks, as shown in Figure 2.10, adaptive according to spatial refinement levels in Cartesian grid, and Fortran 90 and the Message Passing Interface standard for parallel atmosphere models. It also contains an ionosphere model, various upper atmosphere models and inner magnetosphere models and is executed on a massively parallel computer system. BATS-R-US code solves 3 dimensional MHD equations in finite form using Roe's approximate Riemann Solver. It is now a part of the Space Weather Modeling Framework.

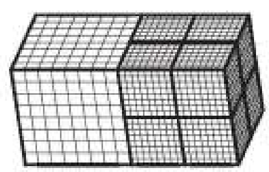

**Figure 2.10:** Self-similar blocks used in block-based adaptive mesh schemes

The model takes

- Solar wind density
- Velocity
- Temperature
- Magnetic field values

as input and gives magnetospheric plasma parameters such as density, pressure, velocity, magnetic field, electric currents, and ionospheric parameters such as electric potential, Hall and Peterson conductance (Toth et al., 2005).

### 2.3. COMPARISONS BETWEEN INTERBALL OBSERVATIONS AND BATS-R-US MODEL RESULTS

Both BATS-R-US and Open Geospace General Circulation Model (OpenGGCM) MHD models of Community Coordinated Modeling Center (CCMC) give snap shots of magnetic field configurations at each 4 min resolution at the highest temporal resolution in addition to the parameter based outputs. One can create contour, vector, streamline, field line plots of the appropriate magnetospheric output parameters. Both OpenGGCM and BATS-R-US models run in study for testing the particle codes and for the two real cusp events, Event 1 and Event 2, which were explained in Section 2.1. As an example, here are the snapshots of the magnetosphere from BATSRUS run for Event 1 and Event 2 presented. Spacecraft position and the concurrent IMF and solar wind parameters were input to the model.

#### 2.3.1 EVENT 1 COMPARISONS

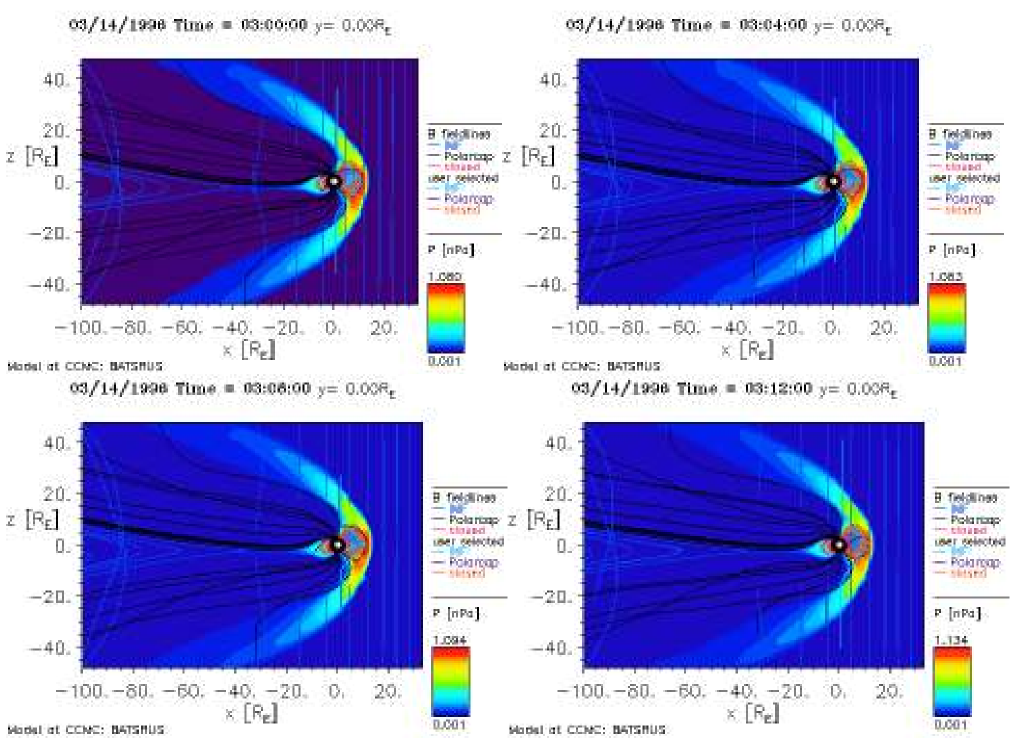


**Figure 2.11:** Snap shots of magnetospheric field configuration from BATSRUS at each 4 min on 14 March 1996 in xz-plane. The colored contours represent the thermal pressure and the lines represent the magnetic field lines in different magnetospheric regions being red as the closed dipole field lines, black as polar cap, and blue as IMF.

Figure 2.11 gives the snapshots of the magnetospheric field configuration in the xz-plane at the beginning of the cusp crossing in March 14, 1996. Color contours show the thermal pressure in nanoPacal (nPa). The dark black circled area is the polar cap area which is excluded in the model run. On this day the IMF had southward magnetic fields and the average solar wind velocity was around 550 km/sec and the density was at about 3 #/cc which resulted in higher than normal dynamic pressures around 2.5 nPa measured at Wind. Due to the southward IMF, the magnetosphere was at compressed stage and substorms are expected to occur owing to high solar activity which created southward solar fields. The tail reconnection seems to occur at about -40 Earth Radii (Re) in the model. Red field lines give the dipole fields which are connected to IMF while the black lines give the open field lines which seen are seen connected to the IMF lines and dragged back into the tail from the polar cap area. Thermal pressure is seen higher throughout the magnetosheath and the highest values are seen at the bow shock at the cusps in these simulation results.

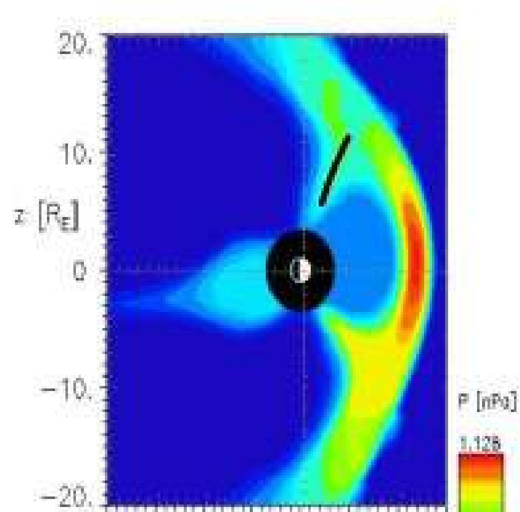


**Figure 2.12:** INTERBALL orbit from 03:08-05:04 UTM on day 14 Mart, 1996 overlaid on the model snap shot in the $XZ_{GSM}$ plane at the beginning of the cusp crossing.

Figure 2.12 shows the Interball trajectory though the cusp on the model snap shot at 03:00 UT, the beginning of the cusp crossing. The spacecraft moves from the lower cusp altitudes into the magnetosheath through the magnetopause and the exterior cusp. At the beginning the cusp area are blue which indicates thermal pressures around 0.4 nPa. However, with time spacecraft encounters higher thermal pressures as it moves through the cusp area.

Figure 2.13 compares the magnetic field variations along the spacecraft trajectory overlaid together from model and from Interball as it moves from the magnetosphere, to cusp, magnetopause, exterior cusp, magnetosheath, bow shock and to the solar wind. The left panels from top to bottom are magnetic field, density, velocity and thermal pressure. The red lines represent the Interball data while pink lines are the model results. Vertical lines delineate the different magnetospheric regions as the spacecraft travels from the magnetosphere out to the solar wind at 11:00 UT. The cusp is seen from 03:08 to 5:04 UT. The right panels give the absolute errors between the model and the observations.

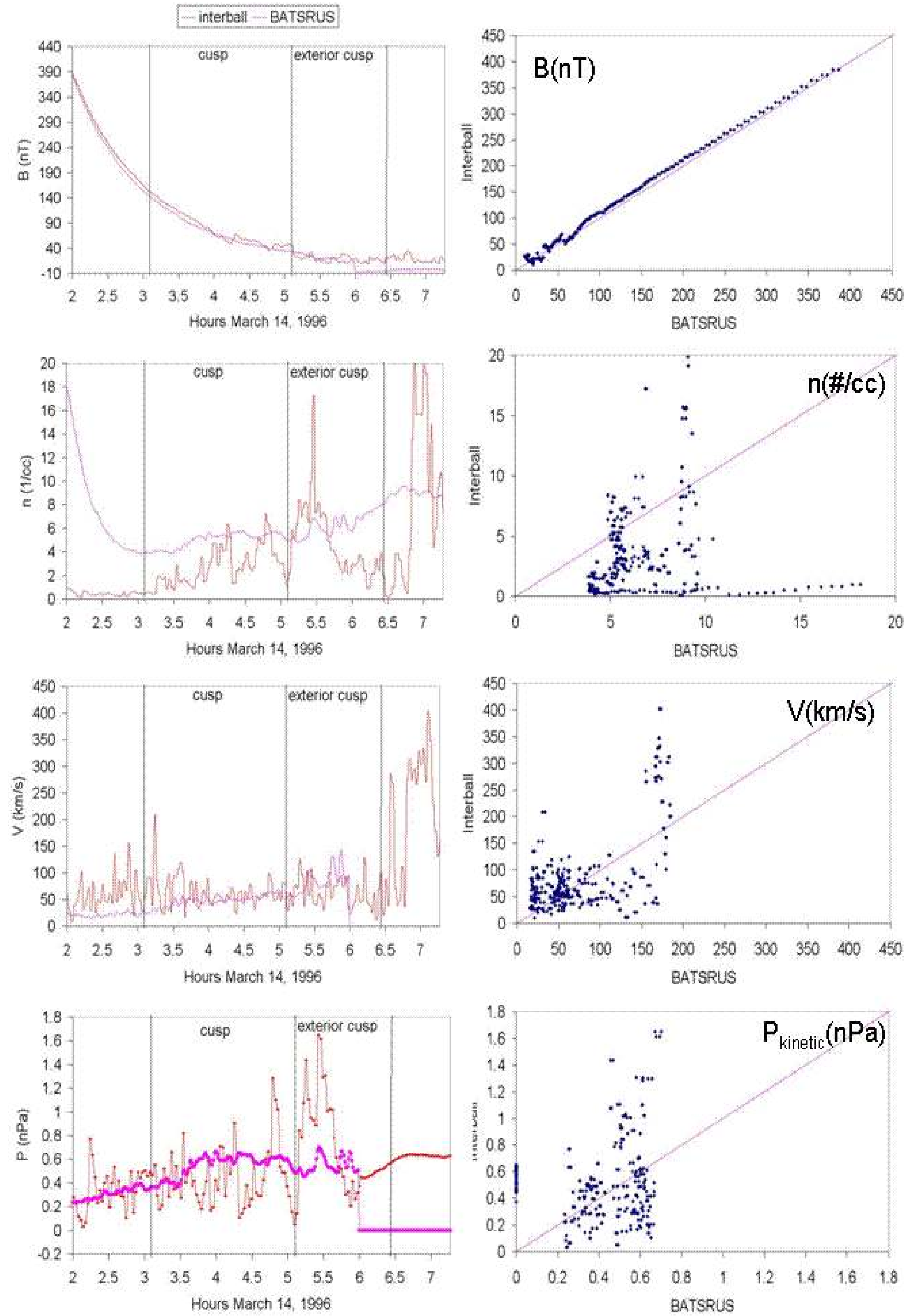


**Figure 2.13:** Magnetic field, density, velocity and thermal pressure comparisons between BATSRUS model output and Interball observations during the cusp crossing from 03:08-05:04 UT for Event1.

In the top panel of magnetic field comparison, it is obvious that the model results closely represent the observed magnetic fields in general while the small fluctuations seen in the cusp and in the exterior cusp are not represented well.

There it is that the model underestimates the observations. This can also be seen in the right panel which shows the absolute errors on the field magnitude. The relation is very close to a linear relation which is shown in pink in the panel. If it were to be a perfect match, all data in this panel will be lie on the pink line. The irregular departures from the pink line seen at the smaller field magnitudes are due to the fluctuating fields in the cusp and exterior cusp. Table 2.1 gives the average and absolute error values between the model and the observations.

**Table 2.1**: Average magnitudes and absolute errors between the model and the data in the cusp region for EVENT 1

| | CUSP<br>03:00-05:04 UT---$65^{o}$-$56.81^{o}$ | | | EXTERIOR CUSP<br>05:04-06:27 UT---$56.81^{o}$-$56.73^{o}$ | | |
|---|---|---|---|---|---|---|
| | Average | Absolute Error | Relative Error (%) | Average | Absolute Error | Relative Error (%) |
| Magnetic field (nT) | 77.59 | 07.95 | 28 | 21.00 | 14.58 | 131 |
| Density (#/cc) | 2.79 | 02.36 | 164 | 04.14 | 03.98 | 396 |
| Velocity (km/s) | 64.52 | 23.05 | 52 | 71.96 | 49.43 | 73.8 |
| Pressure (nPa) | 0.45 | 00.21 | 41.5 | 00.66 | 00.47 | 26.7 |

In the density panel of Figure 2.13, it can be seen that the observed density is lowest in the cusp on average increasing toward the exterior cusp, higher in the exterior cusp. Prior to cusp entry, density is seen to be at zero which is in fact related to the measurement ranges of CORALL instrument, which is design to measure in the magnetosheath type plasma. Observed density fluctuates between 1-6 #/cc. The model results for density are to be much higher and smoother than the observed data. The data average in the cusp is 2.79 #/cc and the absolute error is seen to be 2.36 #/cc. This points that on the average, the model predicts 55% higher values in the cusp. Model density data increase from the entry to the exit from the cusp as a tendency in the data as well but this increase is seen to take place much smoother in the model than in the observations. The model does not catch the variations in data very well but it is seen that some of the variations in the model resembles the variations in the observed density. The quantitative differences are very clear. The right panel showing the absolute errors for density is highly scattered due to the inclusion of the all data for the crossing not only for the cusp region. The absolute error panel on the right for density shows there is a lot of scatter in the data and the data points lie away from the pink line on other wise they would be lie on.

The velocity panel shows that the velocity decreases and stays almost constant within the cusp as the spacecraft moves into the cusp from the magnetosphere. The velocity fluctuates very high. The average velocity in the cusp from Table 2.1 is 64 km/s. Apart from the fluctuations, the model quantitatively resembles the data on the average. Average model velocity within the cusp region is about 50 km/s which results in about 10% difference from the observations. The model seems to resemble the data better in velocity and magnetic field than in density. Same instrumental problem also applies to velocity in the magnetospheric region. The model resembles the data better in the exterior cusp and in the magnetosheath as it catches the variations quite well. Especially in the magnetosheath, model and the data is seen to overlap which shows a good agreement.

The kinetic pressure or the thermal pressure is calculated from P=nkT where n denotes density, k Boltzmann constant and T is the temperature. Last panels compare the variation in observed and model kinetic pressure. On the average, in the cusp, the difference between the model and the data is about 10 %, being the model is higher. The average observed pressure is about 0.4 nPa while in the model it is 0.55 nPa. On the average, the observed pressure increases with some fluctuations owing to the density and temperature variations in the cusp. The model results are smoother but it also shows a general increasing trend resembling thus tendency of the observations in the cusp. The fluctuations, however, caught in the model and quantitative differences are apparent: which is one of the significant disagreements between the model and the data.

### 2.3.2. EVENT 2 COMPARISONS

Figure 2.14 compares the magnetic field measurements with the model magnetic field output. The format of the Figure 2.14 is same in Figure 2.13. The cusp was encountered between 03:24-04:12 UT for Event 2. The IMF and solar wind conditions are given in Figure 2.7 in Chapter 2. There, IMF Bz swings between southward when the spacecraft is in the magnetosphere, northward, except from a very narrow interval of southward at about 3:35 UT, turns southward again when spacecraft is in the exterior cusp. IMF By is negative throughout the crossing so the Earth is in the toward sector. The solar wind dynamic pressure swings around 1.5 nPa.

In the first panel on the left in Figure 2.14, the model predictions are lower than the observed magnetic field by a factor of 0.85 nT. However, it is clear the model predicts even the smaller variations in the magnetic field. Qualitatively model is very successful to produce the variations in the observed magnetic fields.

The density panel shows larger differences both in the cusp and in the exterior cusp regions between the model and observations. Some of the features both in the cusp and in the exterior cusp are in agreement with the observations with a delay. Quantitative agreements are better in the exterior cusp but not in the cusp. The model is much too high in the cusp than the observations.

For velocity, the model is seen to be much successful both qualitatively and quantitatively in the exterior cusp than in the cusp. Still the cusp model results better agree with observations than density. Similar results can also be drawn for the pressure comparisons.  Exterior cusp variations are very caught by the model while the cusp pressure quantitatively in less agreement. Table 2.2 gives the average values, absolute error and relative error between the model and the data.

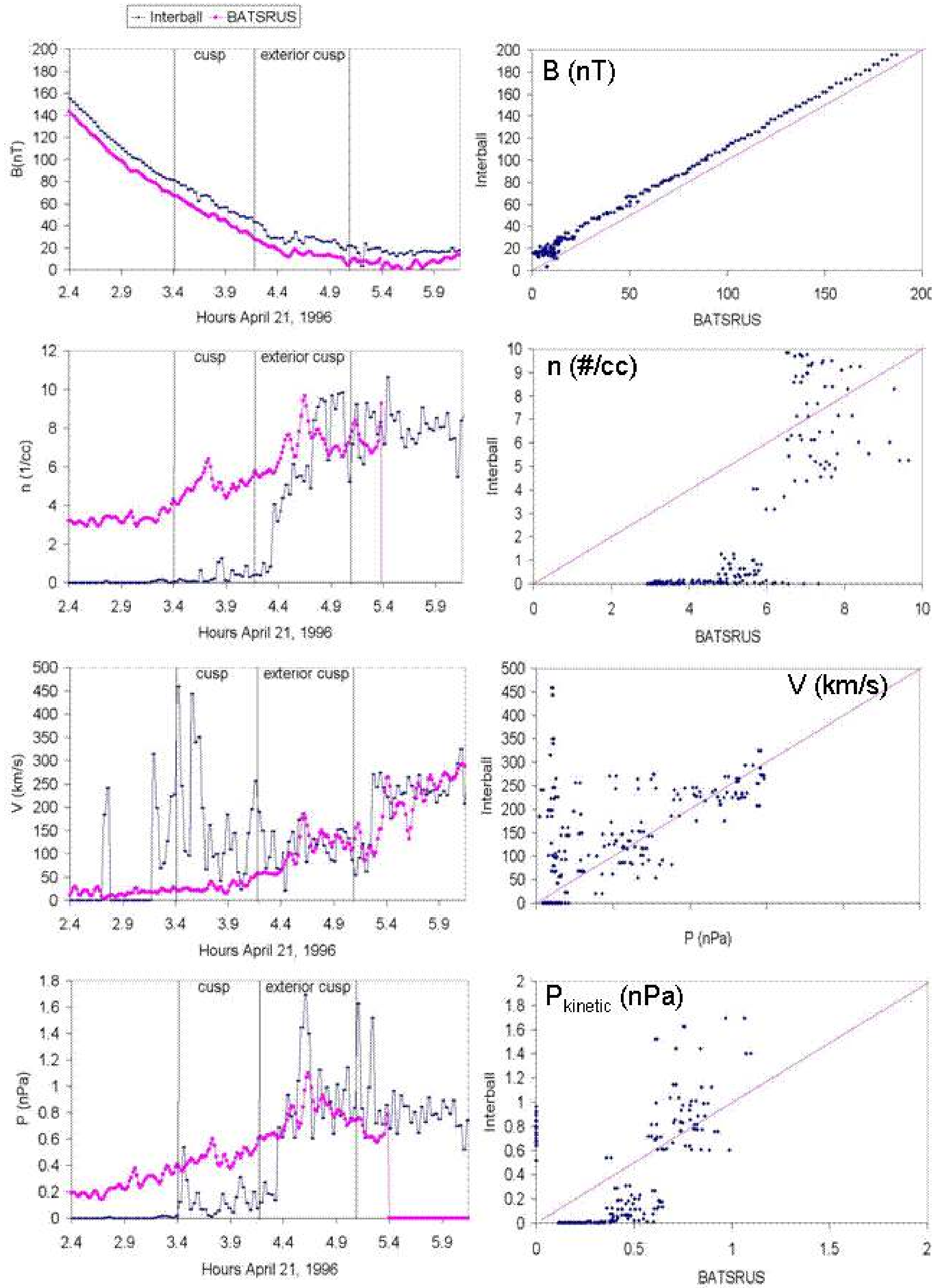


**Figure 2.14**: Magnetic field, density, velocity and thermal pressure comparisons between BATSRUS model output and Interball observations during the cusp crossing from 03:24-04:12 UT for Event2.

**Table 2.2**: Average magnitudes and absolute errors between the model and the data in the cusp region for EVENT2

| | CUSP 03:24-04:12---60.47°-60.5°54. | | | EXTERIOR CUSP 04:12-05:09--- 60.5°-59.82°. | | |
|---|---|---|---|---|---|---|
| | Average | Absolute Error | Relative Error (%) | Average | Absolute Error | Relative Error (%) |
| Magnetic field (nT) | 61.10 | 13.57 | 23 | 27.64 | 12.75 | 47.5 |
| Density (#/cc) | 0.32 | 4.7 | 420 | 5.83 | 2.75 | 165 |
| Velocity (km/s) | 174.8 | 145.9 | 75.32 | 113.56 | 37.87 | 43.8 |
| Pressure (nPa) | 0.13 | 0.34 | 703 | 0.83 | 0.26 | 59 |

## 3. PARTICLE TRACING

Particle tracing is a common method applied in space studies to explore the magnetospheric regions. In their work, Richard et. al. (2002) traced energetic ions of solar origins with different energies to inquire the entry of these particles into the magnetosphere. They found that the IMF controlled the particle's entry into the magnetosphere. The most effectual entries happened under southward IMF**.** Figure 3.1 shows one example, where trapped particle eventually precipitate into the atmosphere.

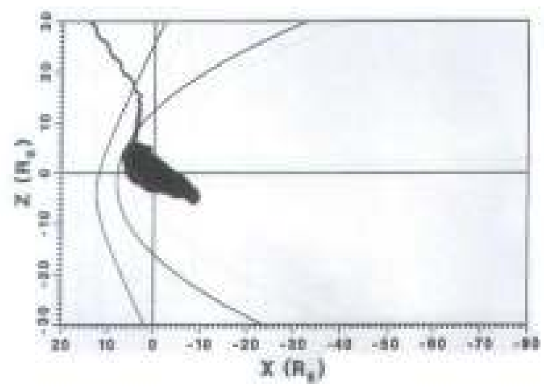

**Figure 3.1.** The particle precipitates into the atmosphere after 10 hours of simulation (Richard et al., 2002).

In this chapter the particle tracing procedures are explained. The main purpose of this study is to develop a code which will, at the end, be run to trace the energetic particles that were seen and presented in Chapter 2. First part in this chapter, the method that is used for the tracing, test the code in uniform fields, test the code in a fixed IMF and solar wind conditions and finally test for two real cases presented in the previous chapter will be described.

## 3.1. METHOD

In this study, Verlet leapfrog method is used. It is a method, where positions and velocities of particles are successively 'leap-frogged' as shown in Figure 3.2 over each other using accelerations calculated from force field.

$$r(t+dt) = r(t) + \mathrm{v}\left(t+\frac{dt}{2}\right)dt \tag{3.1}$$

$$\mathrm{v}\left(t+\frac{dt}{2}\right) = \mathrm{v}\left(t-\frac{dt}{2}\right) + \mathrm{a}\,(t)dt \tag{3.2}$$

Initial velocity $\mathrm{v}_{1/2}$ is calculated from

$$\mathrm{v}_{\frac{1}{2}} = \mathrm{v}_0 + \frac{dtF(r_0)}{2} \tag{3.3}$$

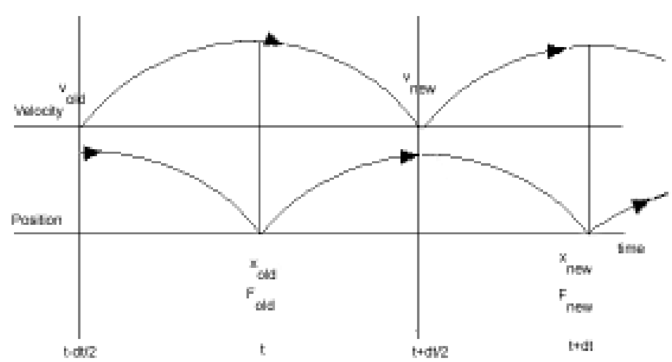


**Figure 3.2:** Sketch of leap-frog integration method showing time-centering of force F while advancing v and of v while advancing x. (Decyk, 1994)

The Verlet scheme has the advantage of high precision, which means that a longer time step can be used for a given level of fluctuations. The Verlet leapfrog method exhibits low drift, which means that the total energy fluctuates about some constant value. The Verlet leapfrog scheme is also symplectic. This means it is time reversible, if the momenta of the particle is reversed at a given time, the particle traces back along its previous trajectory**.** The advantage of symplectic algorithms is that they possess a sort of global stability. This method is also well known to be energy conserving and conditionally stable. Each high energetic particle has very high velocity close to speed of light. In this case relativistic equation of motion should be solved (Omura, 2005).

$$m\frac{d\vec{\mathrm{v}}}{dt} = \vec{F} \tag{3.4}$$

and

$$m\frac{d\vec{r}}{dt} = \vec{\mathrm{v}} \tag{3.5}$$

where $\vec{F} = q\left[\vec{E} + \vec{\mathrm{v}} \times \vec{B}\right]$ (3.6)

For the relativistic generalization of equation, $u = \gamma\mathrm{v}$ is used rather than v. Using the time-centered leapfrog scheme, the equation determining the new velocity $\vec{\mathrm{v}}\left(t + \frac{\Delta t}{2}\right)$ in terms of the old velocity $\vec{\mathrm{v}}\left(t + \frac{\Delta t}{2}\right)$ is given by

$$\vec{u}(t + \frac{\Delta t}{2}) - \vec{u}(t - \frac{\Delta t}{2}) = \frac{q_i}{m_i}\Delta t\,\vec{E}(t) + \frac{\vec{u}(t + \frac{\Delta t}{2}) + \vec{u}(t - \frac{\Delta t}{2})}{2\gamma(t)} \times \vec{\Omega}(t)\,, \tag{3.7}$$

where m is the rest mass and γ is the relativistic corrector,

$$\gamma^2 = 1 + \frac{u^2}{c^2} \tag{3.8}$$

where

$$\vec{\Omega} = \frac{q\vec{B}}{m} \tag{3.9}$$

is the vector cyclotron frequency. Writing this out in terms of the three components of $\vec{v}$, one obtains three algebraic equations in three unknowns. In the first place relativistic effect is added to the velocity.

$$\vec{u}(t-\frac{\Delta t}{2}) = \frac{c}{\sqrt{c^2 - \left|\vec{v}(t-\frac{\Delta t}{2})\right|^2}}\vec{v}(t-\frac{\Delta t}{2}) \tag{3.10}$$

Relativistic effect is also added in the magnetic field. Acceleration at t is calculated.

$$\vec{B}_u(t) = \frac{c}{\sqrt{c^2 + \left|\vec{u}(t-\frac{\Delta t}{2})\right|^2}}\vec{B}(t) \tag{3.11}$$

$$\vec{u}(t\_1) = \vec{u}(t-\frac{\Delta t}{2}) + \frac{q}{m}\frac{\Delta t}{2}\vec{u}(t-\frac{\Delta t}{2}) \times \vec{B}_u(t) \tag{3.12}$$

This acceleration is used to calculate the velocity at t= $(t+\frac{\Delta t}{2})$.

$$\vec{u}(t\_2) = \vec{u}(t\_1) + \frac{2}{1+\left(\frac{q\Delta t}{2m}\vec{B}_u(t)\right)^2}\vec{u}(t\_1) \times \frac{q\Delta t}{2m}\vec{B}_u(t) \tag{3.13}$$

Relativistic effect is added to the velocity at t= $(t+\frac{\Delta t}{2})$.

$$\vec{v}(t+\frac{\Delta t}{2}) = \frac{c}{\sqrt{c^2 + \left|\vec{u}(t\_2)\right|^2}}\vec{u}(t\_2) \tag{3.14}$$

The new positions $\vec{r}(t+\Delta t)$ are given in terms of the old positions $\vec{r}(t)$ by the expression (Decyk, 1994):

$$\vec{r}(t+\Delta t) = \vec{r}(t) + \vec{v}\left(t+\frac{\Delta t}{2}\right)\Delta t \,. \tag{3.15}$$

## 3.2. TESTS FOR PARTICLE TRACING CODE

### 3.2.1. Test with Uniform fields

A particle that moves under the influence of a uniform magnetic field will move on a gyrating spiral trajectory along the magnetic field line. The test particle was placed in a 10nT uniform magnetic field parallel to the z-axis with initial position x=0, y= 0 and z=0.55Re. Its initial velocity was chosen as $V_x$=45km/s, $V_y$=0, $V_z$=-6km/s. The code in this case solves only $\frac{d\vec{V}}{dt} = q(\vec{V} \times \vec{B})$. Tracing in the code stop when either the particle encounter the model boundaries which located at 30 to -30 Re in x, y, and z-directions or when the particle falls into the atmosphere or when the time steps exceed the step number defined within the code. Particle trajectory with both time steps defined by the gyro period at the initial position that particle passes and kept constant throughout the run and the time steps changing at each step with the gyro period that the particle will have, were tested. Figure 3.3 gives the particle's trajectory with code run for 200 time steps and gyro period of 0.017 second.

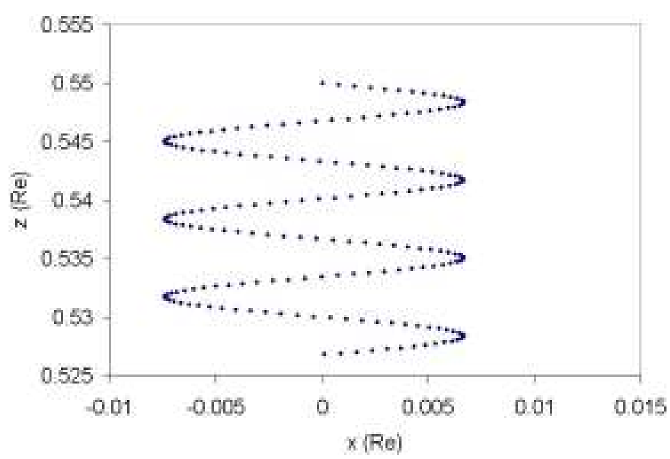


**Figure 3.3:** Particle's trajectory in a uniform magnetic field aligned parallel to the z-axis.

A particle moving under the effect of an electric field alone moves and accelerates along the electric field direction. The equation of motion in this case is $\frac{d\vec{V}}{dt} = q\vec{E}$.

The test particle is placed in a 0.00045V/m uniform electric field aligned parallel to x-axis with initial position x=0, y= 0and z=0.55Re. Its initial velocity was $V_x$=45km/s, $V_y$=0, $V_z$=0. Its trajectory, which is parallel to electric field line, is shown in Figure 3.4. In this figure, only some part of the trajectory is shown at the beginning of the run.

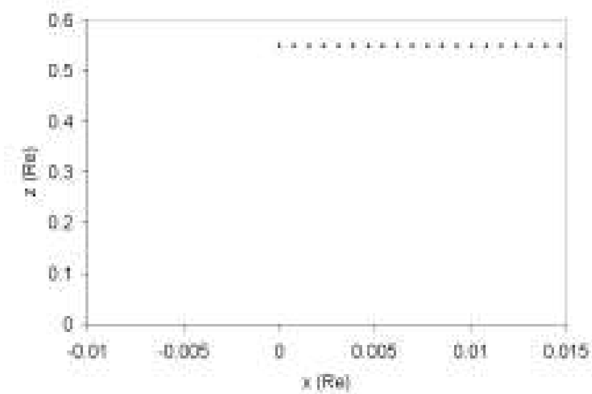


**Figure 3.4:** A particle moving only on a uniform electric field. The electric field is chosen parallel to x-axis.

When both magnetic field and electric fields are present, the trajectory of the particle will move in a direction which is both perpendicular to magnetic field and electric field. The code in this case solves the equation of motion which becomes $\frac{d\vec{V}}{dt} = q\vec{E} + q(\vec{V} \times \vec{B})$. Test particle in this case was placed in an environment where both 10nT uniform magnetic field parallel to z-axis and 0.00045V/m uniform electric field parallel to x-axis are present. Initial position of particle was x=0, y= 0and z=0.55Re, with initial velocity was $V_x$=45km/s, $V_y$=0, $V_z$=-6km/s. The trajectory of this particle is shown in Figure 3.5. The trajectory is in the xy-plane.

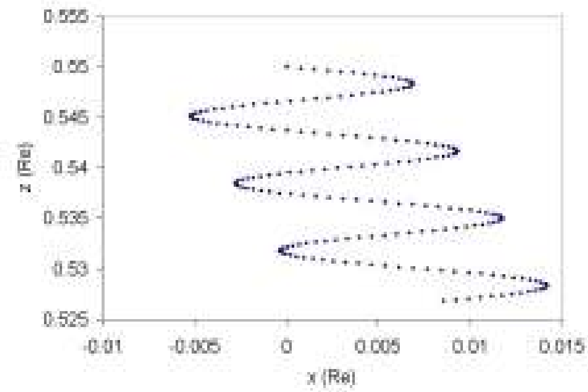


**Figure 3.5:** Particle is moving in a uniform magnetic field and uniform electric field. Electric field lines are parallel to x-axis and magnetic field lines are parallel to z-axis.

### 3.2.2. Testing the Electric Field Dependence of the Motion of Energetic Particles Moving in Uniforms Fields

To investigate electric field's effect on energetic particle's trajectory, particles with initial energies 1eV, 1keV, 10keV and 1MeV are traced in a uniform magnetic field, and electric field. Then these trajectories were compared to those obtained in the absence of electric field but presence of the magnetic field. The energy of the particle has been changed from 1 eV to 1MeV and it is watched how the trajectory of these particles change. It is seen that the electric field looses its effect on the trajectory of the energetic particles as the particle's energy increased and trajectory approaches to that under the effect of only magnetic field without electric field.

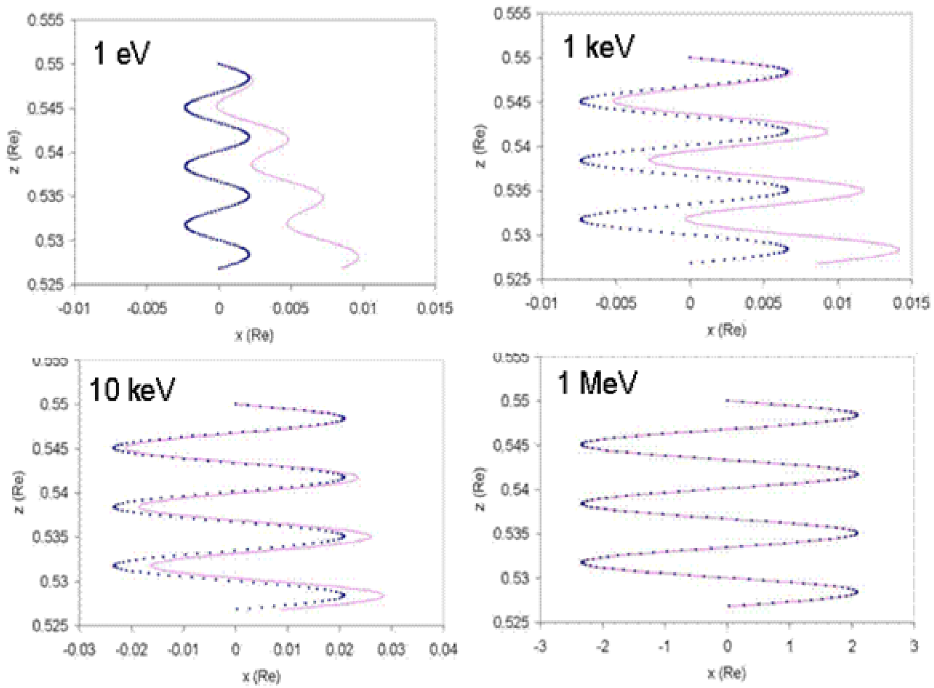


**Figure 3.6:** Red line is the trajectory of a particle with energies of 1 eV, 1 keV, 10 keV, and 1 MeV moving in the presence of magnetic and electric field. Dashed blue line shows the trajectory of the same particle moving in a uniform magnetic field only.

For the test, the initial position of the particle is taken as x=0 y=0 z=0.55Re. The time step is 0.11 seconds and tests are run for 200 steps. Figure 3.6 shows the effect of electric field on the trajectory of the particles. Panels give the trajectories from left to right for particles with energies changing from 1 eV to 1 MeV. Red line gives the trajectory with electric field and the blue line without it. For these conditions, it is seen that the electric fields are not important for particles with energies above 1 MeV. Therefore, in calculations the electric field term was omitted.

The equation of motion used in particle tracing then becomes $\frac{d\vec{V}}{dt} = q(\vec{V} \times \vec{B})$. This result agrees with Sheldon et. al., (1998), who states that high energy particle's trajectory, is directed by magnetic field configuration.

### 3.2.3. Tests for Dipole fields

If there is a field-aligned gradient of the field strength, as it is in the case of dipole field, the component of velocity parallel to the magnetic field decreases as the particle moves into regions of increasing magnetic field magnitude, in this case the

Polar Region. Eventually, the parallel velocity reverses. The reflection of the parallel motion is called “magnetic mirroring”. Motion between the mirror points is called “bounce motion” (Kaymaz, 2006). Thus while particle spirals around the dipole field it also makes its bounce motion between the Earth’s mirror points. This motion is illustrated on the left of Figure 3.7. Several tests were made; the right panel is given to show the particle tracing’s result for comparison to the left panel.

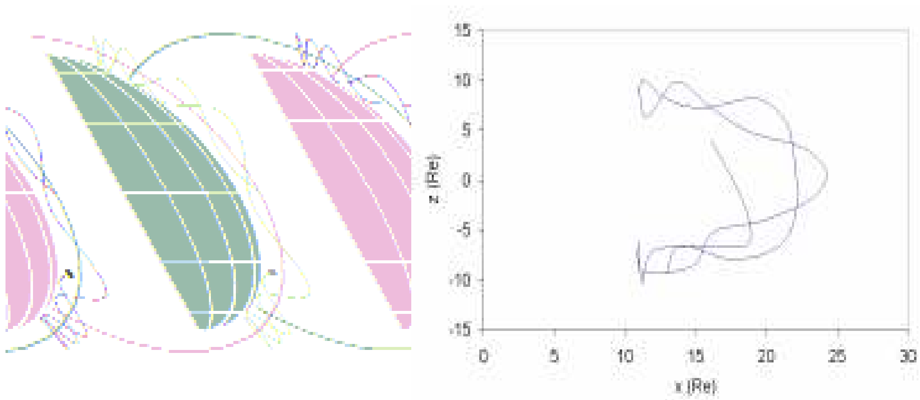


**Figure 3.7:** Mirroring and bounce motion of a particle in a dipole field.

For this, particle starting at initial positions of x=5 Re, y=-5 Re and z=5 Re, with initial velocities $V_x$=450 km/s $V_y$=0 $V_z$=0 was traced in the dipole field. The time step is 5 second and 35 steps were taken. The particle’s gyrating and mirroring between two points is shown in Figure 3.7. The test particle successfully bounces and gyrates around the mirror points. These can be more clearly seen in Figure 3.8 below. The panels in Figure 3.10 gives the one bouncing cycle (left) and half cycle (right) along the dipole field. The particle start at x=0.55, y=-2.81, z=3.4 Re. The particle code for this example was run for initial conditions of Vx=450 km/s, Vy=-12.81, Vz=-6.8 km/s and B=566 nT which gives a gyro frequency and gyroperiod of 59 (#/cc) and 0.017 sec. On the right panel, it is clear that the particle also gyrates with a gyro frequency as it moves along the field.

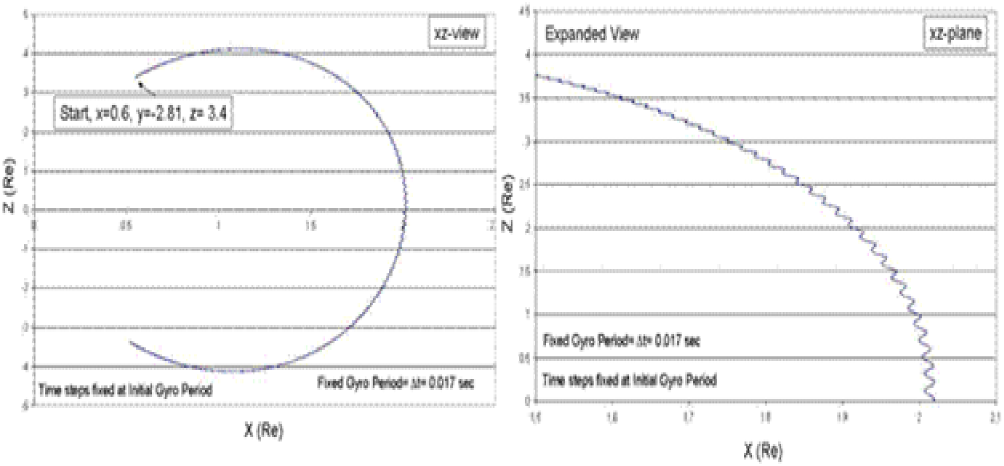


**Figure 3.8:** Result of particle tracing code for one bouncing cycle (left) and half a cycle (right) showing that the particle both moves along the field and gyrates about.

When the particle code is run long enough, then one can see that the particle can move onto a different dipole field on the same L shell. Figure 3.9 partially illustrates this motion. If the code is run in much longer time then it is possible to see this drifting motion**.** Figure 3.10 illustrates the drift motion of the particle as it moves on the same L shell but different dipole field lines.

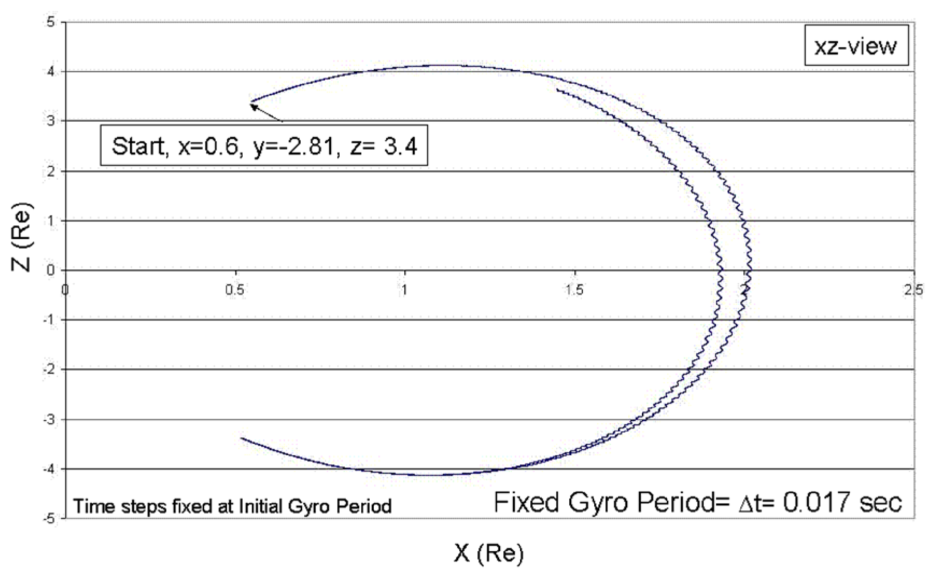


**Figure 3.9:** Particle motion showing the particle's jump onto another dipole field line on the same L shell which will eventually be resulted in the drift motion of the particle around the Earth**.**

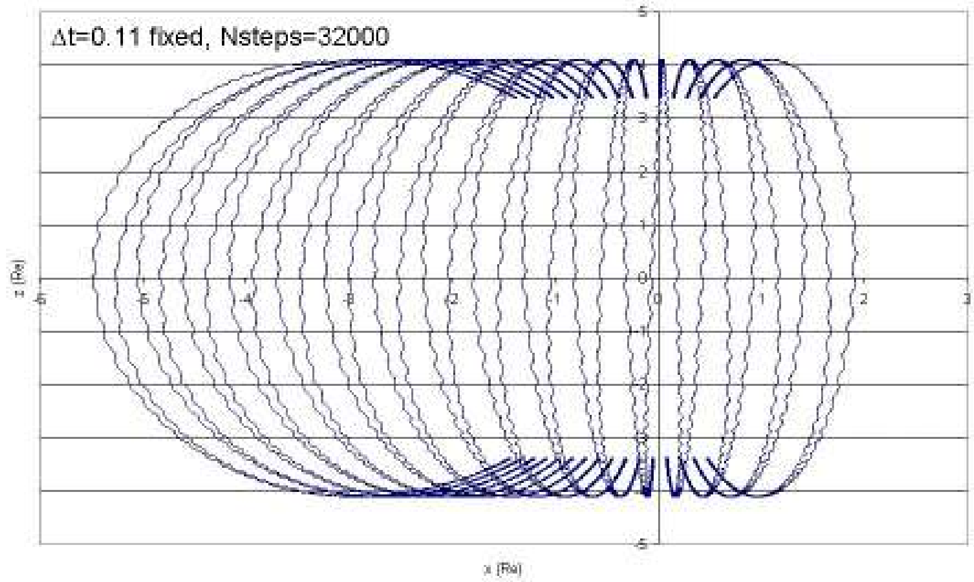


**Figure 3.10:** Code result for the drifting motion of the particle on shell L=9 in xz-plane.

If one can plot particle's position on the equatorial plane each time it crosses the equatorial plane, the particle can be seen as drifting on a circle whose center is at Earth. It is shown in Figure 3.11. While particle gyrates and bounces it also moves around the Earth which called drift motion. In this case in Figure 3.11, the particle drifts on L=9 shell.

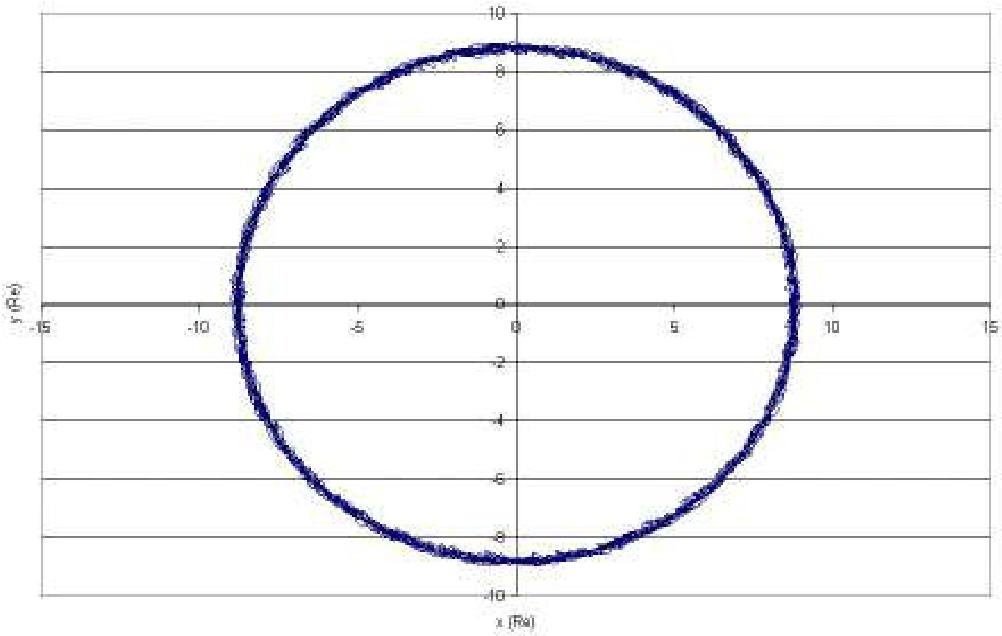


**Figure 3.11:** Code result for the drifting motion of the particle on shell L=9 on the equatorial plane (xy-).

As result, these tests show that the developed particle code produces the particle motions expected from the theory. Next is the test, where the particle moves in the magnetosphere, a real situation.

### 3.2.4. TESTS IN A REAL MAGNETOSPHERE FOR FIXED IMF AND SOLAR WIND CONDITIONS-OPEN GGCM Runs

To test the particle tracing code in a real magnetosphere, CCMC models at NASA were used. OpenGGCM model for pure northward and southward IMFs and moderate solar plasma conditions, which will be described in detail below, is run. MHD model results are used to initialize and to push the particle forward or backward at each step. Several starting points in different magnetospheric regions were tested to see where to or where from the particles come or go when the particle tracing code is run and at each time the appropriate initial conditions were used from the MHD model results. The model's output resolution is 4 min at the highest. Therefore the nearest model results were interpolated temporarily and spatially to the particle position at each time the particle moves onto. Below are the results from these runs presented.

#### 3.2.4.1. Tests for Northward IMF

For northward IMF, OpenGGCM model was run for 8 hours with the IMF and plasma conditions: IMF $B_x$=0 nT, IMF $B_y$= 0 nT, IMF $B_z$=10 nT, n=10 #/cc, $V_x$=-450km/s $V_y$=0 km/s, $V_z$=0 km/s. Dipole tilt in X-Z Plane is -29.5° and dipole tilt in Y-Z GSE Plane is 15.2°. The resulting magnetospheric configuration of the OpenGGCM model for these conditions is given in Figure 3.12. It is a snapshot from the model at time 01:00, the start of the model run time. Due to the dipole tilt, magnetosphere lies below the equatorial plane.

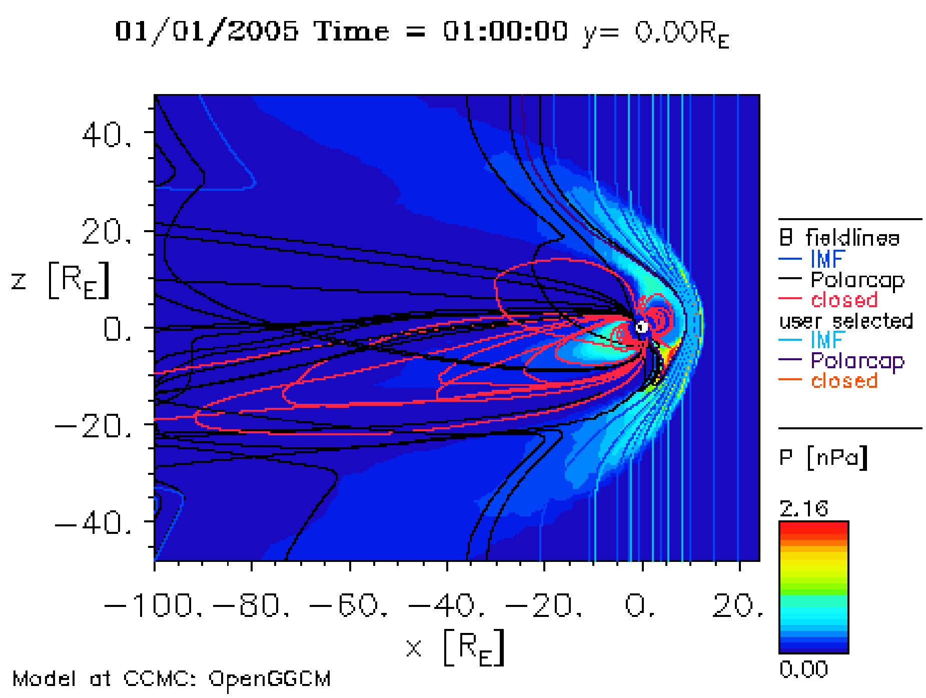


**Figure 3.12:** Magnetospheric configuration from OpenGGCM model run with northward IMF condition.

Tracing has been performed under these conditions using the results from northward run of OpenGGCM. The control box in the particle tracing code was chosen with boundaries from –30Re to 30Re in x, y and z direction. Particle tracing was stopped whenever a particle went out of this control box. Results of the tracing are given in Figure 3.13.

To see particle trajectories in solar wind, particles with 107 keV at initial position x=15Re, y=-4 Re and z=30Re were traced forward. The particle's motion was directed by IMF $B_z$ and it went out of the control box. Next, particle with energy of 4.5MeV was traced with initial position x=15Re, y=-14 Re and z=9 Re. As presented in Figure 3.13a, it also leaves the control box. In the tracing results, the energy of particle increases the gyroradius of the particle increases. While the particle with energy of 107 keV moves on a radius of 0.15 Re, particle with energy of 4.5 MeV particle moves with a gyroradius of 7.41 Re. Table 3.1 below gives the results of the forward tracing code.

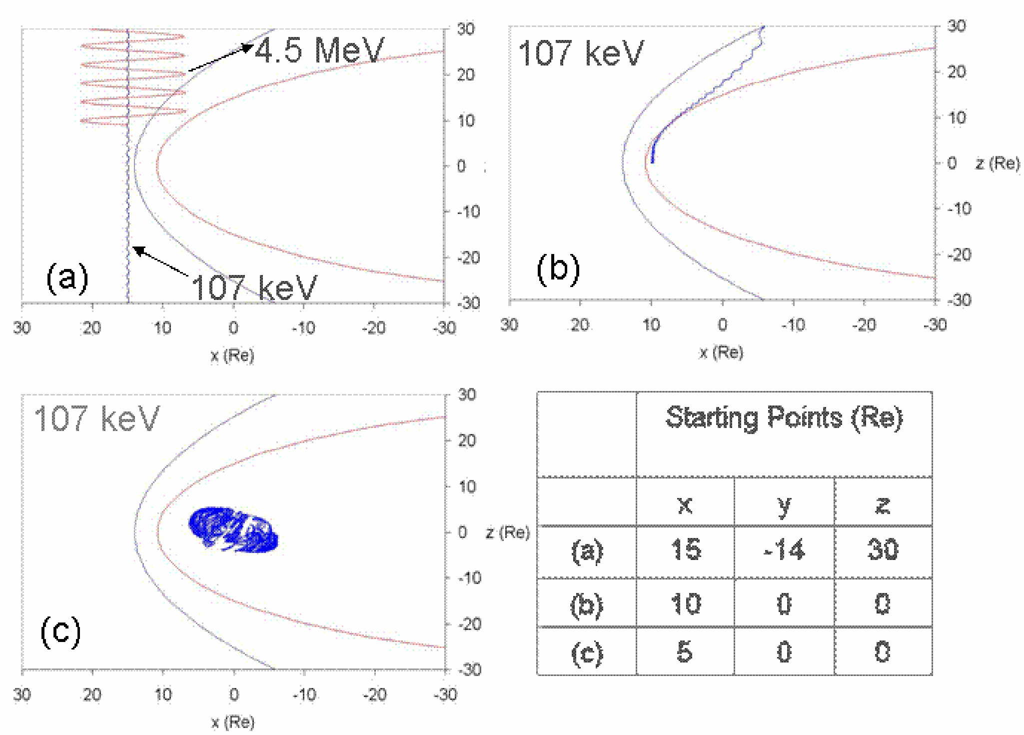


| | Starting Points (Re) | | |
|---|---|---|---|
| | x | y | z |
| (a) | 15 | -14 | 30 |
| (b) | 10 | 0 | 0 |
| (c) | 5 | 0 | 0 |

**Figure 3.13**: Results of tracing code for particles with different energies and initial positions in the solar wind (a), at the subsolar point (b), within the magnetosphere (c). Inserted table is given for particle with 107 keV. The IMF is northward.

**Table 3.1**: Results of the forward tracing for a particle with 107 keV

| Particle with 107 keV<br>OpenGGCM with Northward IMF | |
|---|---|
| Start at | Move to |
| Solar Wind | Solar Wind |
| Subsolar Point Magnetopause | Out Box into the solar wind |
| Magnetosphere | Trapped |

### 3.2.4.2. Tests for Southward IMF

For southward IMF, OpenGGCM model run with following IMF and solar wind plasma conditions of: IMF $B_x$=0 nT, IMF $B_y$= 0 nT, IMF $B_z$=-10 nT, n=10 #/cc, $V_x$=-450 km/s $V_y$=0 km/s, $V_z$=0 km/s, and T=200000 K. The model was run for 8 hours. Dipole Tilt in X-Z Plane is -29.5 deg and in Y-Z GSE Plane is 15.2 deg. The snapshot of the magnetospheric configuration at the beginning of the run is presented in Figure 3.13. Compared to the northward IMF case in Figure 3.11, the magnetosphere is compressed more on the dayside, magnetospheric tail is smaller and the magnetosheath thickness is smaller as well. Color contours show the pressure contours. The maximum pressure is 3.33 nPa for southward IMF while it 2.2 nPa for northward. The field lines, especially the closed field lines shown in red are long and extended beyond -100 Re in the northward IMF case while they are more bend toward the tail's axis in the southward IMF case. More black lines which are the indicative of open fields coming out of the polar caps are more in the southward IMF case than in northward. These indicate that the magnetosphere is disturbed during the southward IMF case.

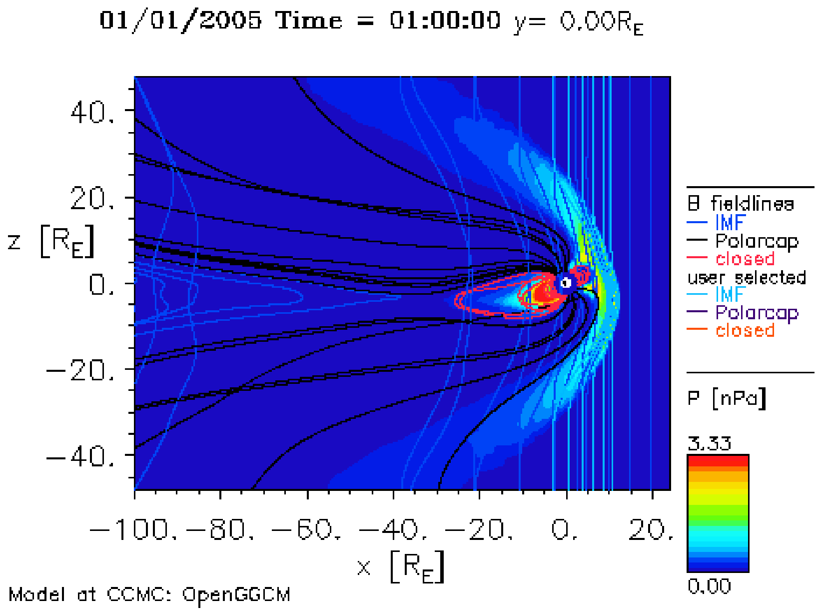


**Figure 3.14:** Magnetospheric configuration from OpenGGCM model run with northward IMF condition.

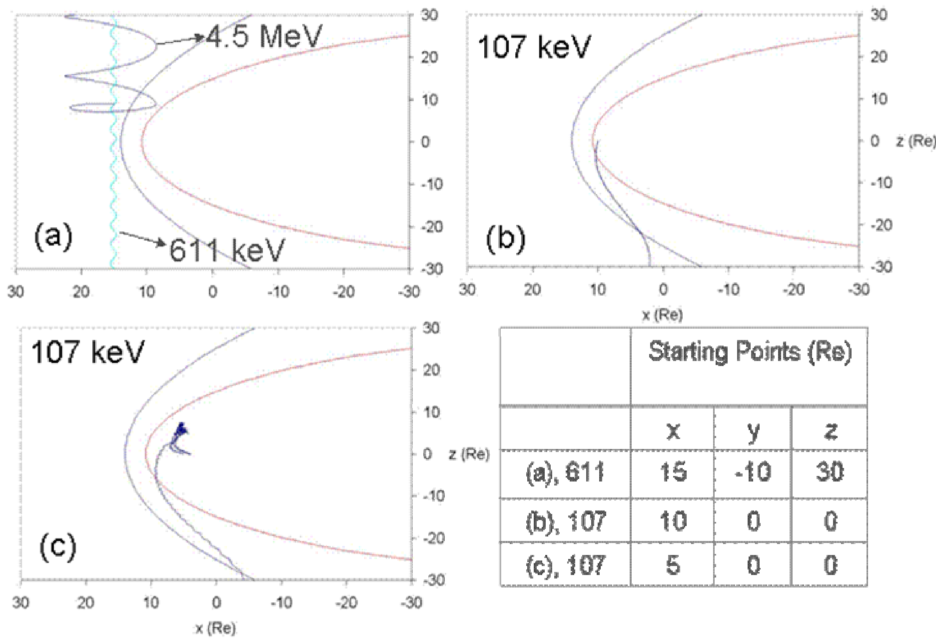


| | Starting Points (Re) | | |
|---|---|---|---|
| | x | y | z |
| (a), 611 | 15 | -10 | 30 |
| (b), 107 | 10 | 0 | 0 |
| (c), 107 | 5 | 0 | 0 |

**Figure 3.15**: Results of tracing code for particles with different energies and initial positions in the solar wind (a), at the subsolar point, near magnetopause (b), within the magnetosphere (c). The IMF is southward.

Particles with initial energy of 611 keV and 4.5 MeV were traced in southward IMF. Initial position of 611 keV particle is x=15Re, y= -10 Re and z= -30Re. 4.5 MeV particle was released from the same position as in northward case. As shown in Figure 3.15a, both particles stayed in the solar wind. The gyroradius of 611 keV particle is 0.61 Re.

The second particle with energy 107 keV at the subsolar point near the magnetopause was traced as in the northward IMF as given in Figure 3.15b. Particle went out of the box following south, in the direction of the IMF. In the case of northward IMF, particle leaves the box northward direction which is the direction of IMF. These exercises illustrate the particles trajectory dependence on the IMF direction.

As last example, particle with initial position x=5 Re, y=0 and z=0 was traced within the magnetosphere. In northward IMF case, it was trapped in magnetosphere, as presented in Figure 3.13. In southward case, it remains trapped for a short time but then leaves the control box as seen in Figure 3.15c.

As a conclusion particle with various energies were traced in solar wind and tracing results agree with theoretical expectations in the solar wind. Particles near magnetopause, in magnetosphere and in solar wind were traced. In northward case particle in magnetosphere remained trapped while that in southward case leaved the control box. This difference results due to the different magnetospheric states and the reconnection occurring on the dayside and the high probability of substorms in the tail region. Although further analysis is needed to address the differences, here is only differences from the tracing point of view is concerned. Deep physical explanations will not be given at the moment. However, the differences are clear in both cases. Due to reconnection process during the southward IMF, the fact that closed magnetic field lines become open controls the particles path. In Figure 3.16, particle trajectories in northward and southward were compared.

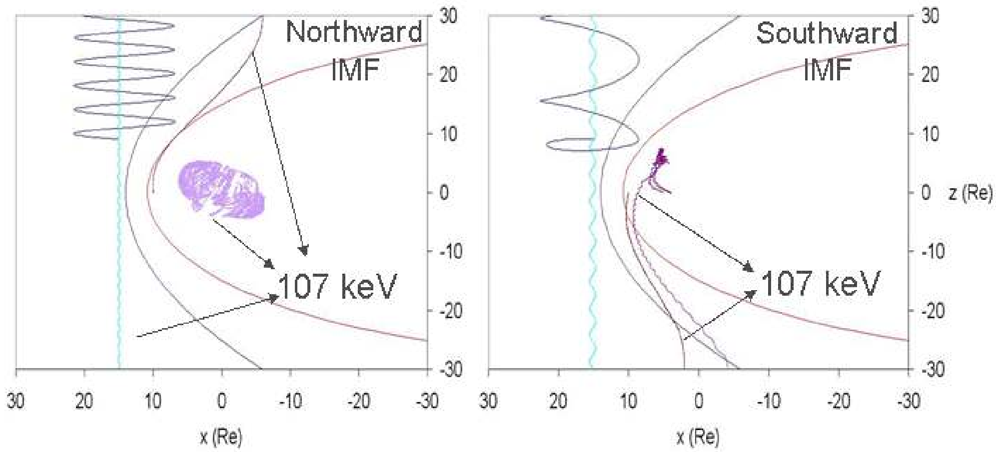


**Figure 3.16:** Comparison of particle trajectories for northward and southward IMF conditions

### 3.3. PARTICLE TRACING FOR CHANGING IMF AND SOLAR WIND CONDITIONS

In this part, particles for the events described in Chapter 2 are traced. BATS-R-US model results for Event 1 and Event2 are used to trace energetic particles backward in cusp. To remember, Event 1 and Event 2 correspond to 14 March 1996 and 21 April 1996 respectively. Both events are taken from (Pissarenko et al., 2001). The INTERBALL trajectories for the entire pass overlapped on the magnetospheric configuration from BATS-R-US in Figure 3.17. This figure gives the slab of the magnetosphere in the xz-plane. Square darker dots on the trajectory shows the cusp region as the spacecraft moves. Color contours represent again the kinetic pressure. The stronger pressure region through the cusp funnel can be seen. To remind here, the IMF was southward during the Event 1 and northward during the Event 2 cusp crossing from, in both cases start around 03:00 UT and to 05:08 UT in Event 1 and to 04:12 UT in Event 2.

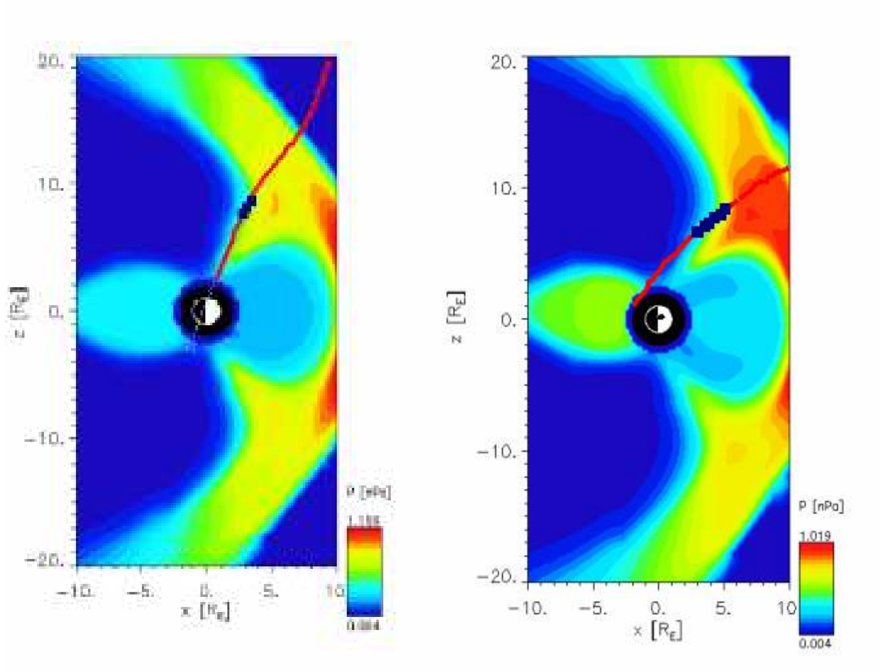


**Figure 3.17**: INTERBALL Trajectory overlapped on the magnetosphere from BATS-R-US during Event 1 (left) and Event 2 (right).

### 3.3.1. Tracing Results for Event 1

Particles with energies of 21-27 keV and 1 MeV-3 MeV, which correspond to the energy ranges of DOK-2 instrument on INTERBALL, at starting positions, taken at each hour, were used for tracing. The starting position of the particle here is expressed in local time. The results are presented in Figure 3.18 and Figure 3.19.

A particle with initial energy of 21 keV is traced at first. Particle was released from the spacecraft position at 3 a.m. During this period southward $B_z$ component of IMF was dominant. After 5725 iterations with 0.11-second step time, the particle left the control box in the nightside tail. In this case, as seen in Figure 3.18a, the origin of this particle is recognized as magnetospheric tail. A particle with initial energy of 27 keV left the control box through the magnetosheath out to the solar wind after 2566 iterations with 0.11-second step time (Figure 3.18b). In this case the particle come from the solar wind can be said. A particle with initial energy of 1 MeV became immovable in the magnetosphere after 205 iterations with 0.11-second step time (Figure 3.18c). A particle with initial energy of 3 MeV after 117 iterations with 0.11-second step time the particle left the control box into the solar wind (Figure 3.18d). In this case the particle's origin is acknowledged as solar wind.

The right panels in Figure 3.19 present the tracing results at the end of the cusp crossing at 05:00 UT. From the panels, it can be seen that the all particles are traced back to the magnetosheath when they exit the control box.

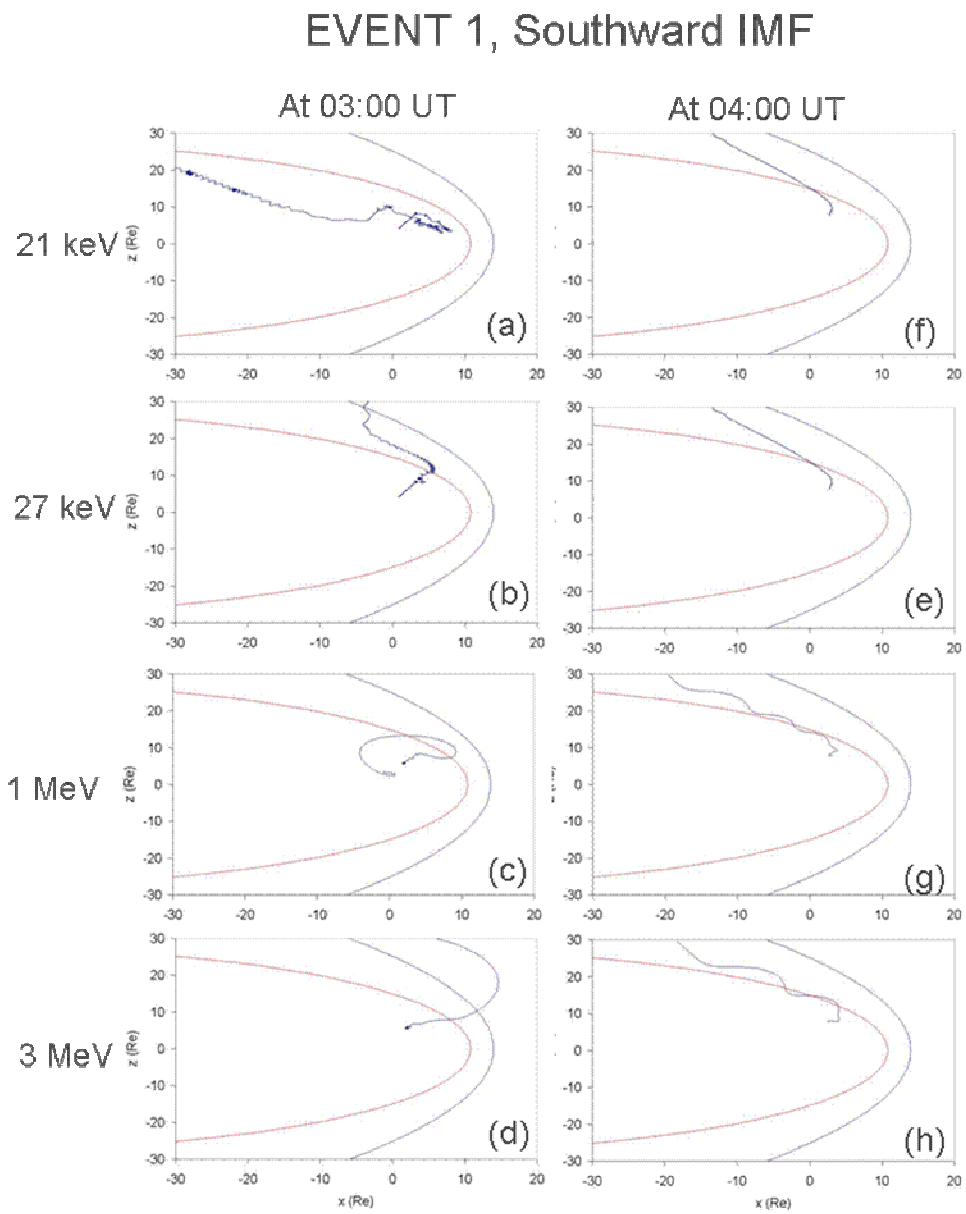


**Figure 3.18:** Results of tracing codes for particles with different energies in the cusp for Event 1 at 03:00 and 04:00 UT starting times.

The trajectories of the particles at 05:00 and 06:00 UT are given in Figure 3.18. Table 3.2 summarizes this run's results.

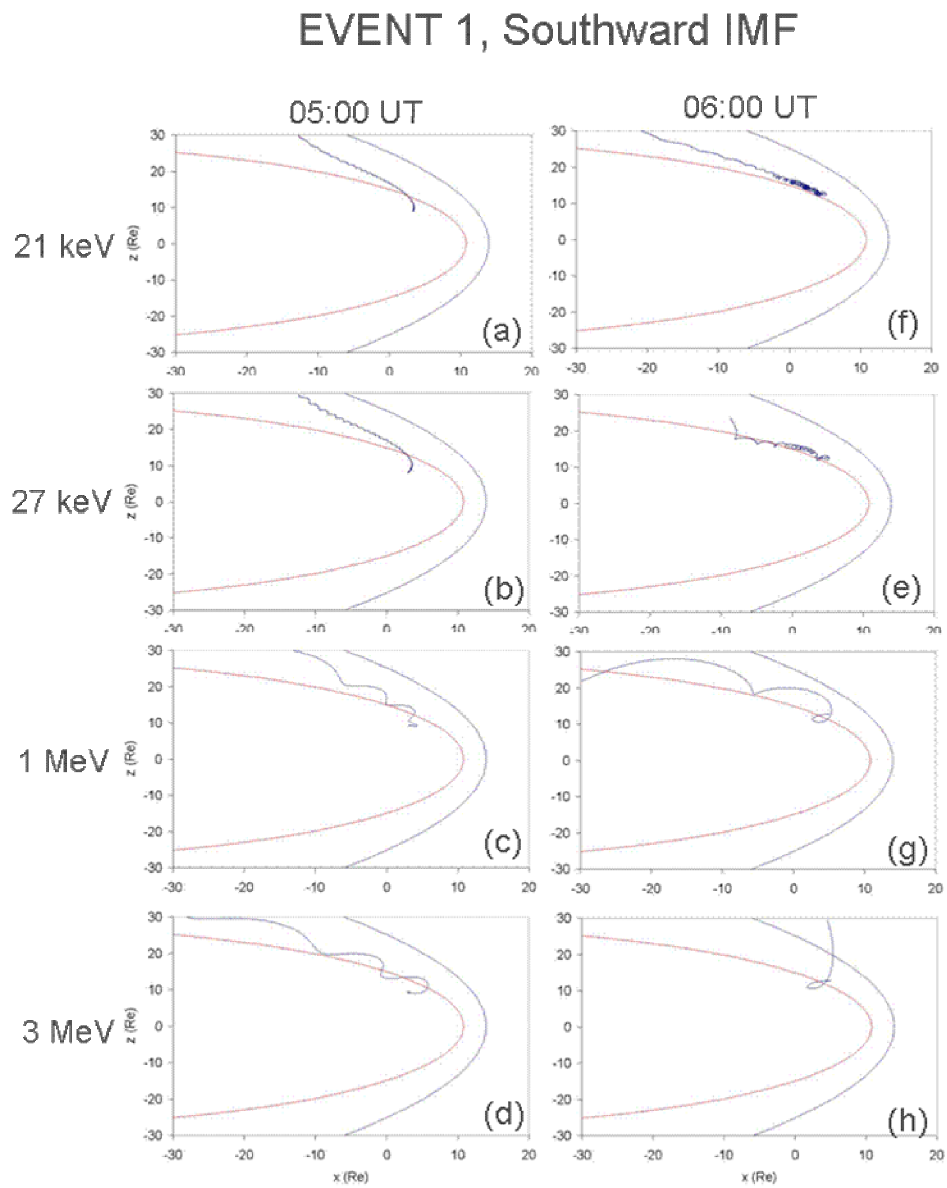


**Figure 3.19:** Results of tracing codes for particles with different energies in the cusp for Event 1 at 05:00 and 06:00 UT starting times.

**Table 3.2**: Summary of the backward tracing for Event 1

| EVENT 1 | 21 keV | 27 keV | 1 MeV | 3 MeV |
|---|---|---|---|---|
| 03:00 | Magnetic tail | Solar Wind | Magnetosphere | Solar Wind |
| 04:00 | Magnetosheath | Magnetosheath | Magnetosheath | Magnetosheath |
| 05:00 | Magnetosheath | Magnetosheath | Magnetosheath | Magnetosheath |
| 06:00 | Magnetosheath | Magnetopause Boundary | Magnetosphere | Solar Wind |

### 3.3.2. Tracing Results for Event 2

In the second event, Event 2, IMF was northward during cusp crossing. Test particles were released in the same procedure as in Event 1 described in the previous section. Figure 3.20 and Figure 3.21 give the results of tracing at 03:00, 04:00 UT and 05:00. These times are used to initialize the particle position and other parameters.

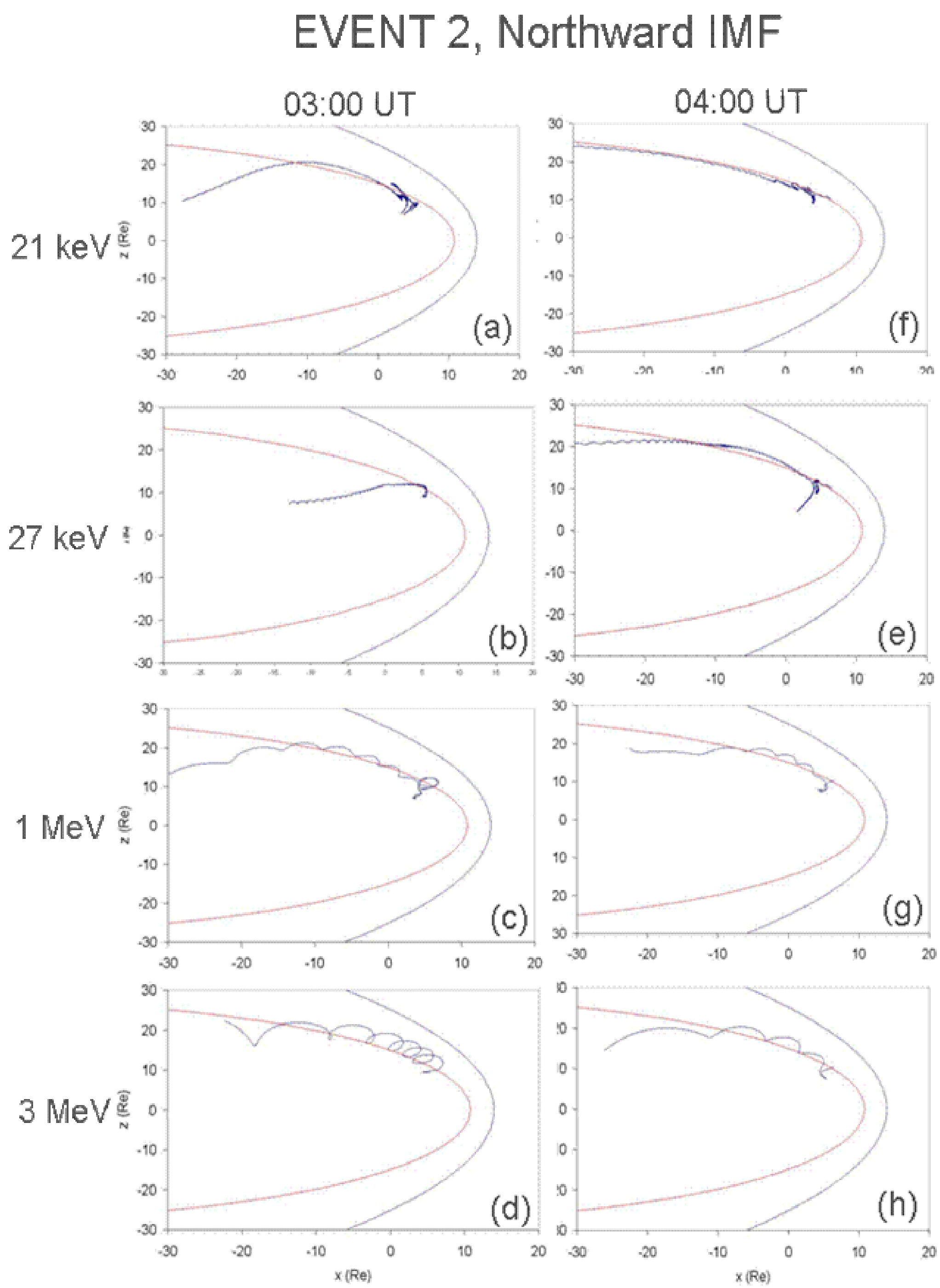


**Figure 3.20:** Results of tracing codes for particles with different energies in the cusp for Event 2 at 03:00 and 04:00 UT starting times.

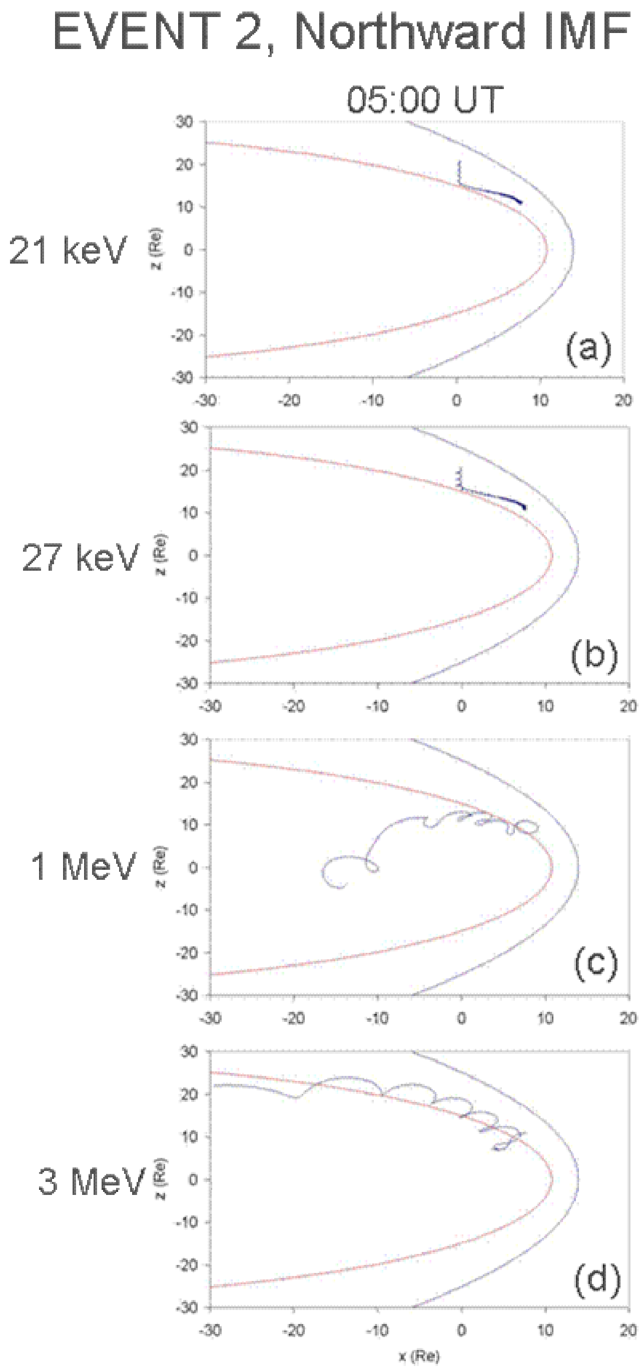


**Figure 3.21:** Results of tracing codes for particles with different energies in the cusp for Event 2 at 05:00 UT starting time.

**Table 3.3**: Summary of the backward tracing for Event 2

| EVENT 1 | 21 keV | 27 keV | 1 MeV | 3 MeV |
|---|---|---|---|---|
| 03:00 | Magnetosphere (Magnetopause) | Magnetosphere | Magnetosphere (Magnetopause) | Magnetopause (Magnetosheath) |
| 04:00 | Magnetopause | Magnetosphere (Magnetopause) | Magnetosphere (Magnetopause) | Magnetosphere (Magnetopause) |
| 05:00 | Magnetosheath | Magnetosheath | Magnetosphere | Magnetosphere (Magnetopause) |

### 3.4. STATISTICS

Table 3.4 evaluates the results of the particle tracing for two events together. From these 28 cases, the average stay time in the control box was found to be 3.46 minutes. The average stay time for particles with 3 MeV energies is 16 seconds. That for particles with 1 MeV is 28 seconds. 27 keV energetic particles' average duration of stay in the control box is 5 minutes. 8 minutes is the average stay period for particles with 21 keV. The shortest stay in the control box was seen during Event 1 at 6$^{th}$ hour for 3 MeV particles. The longest stay occurs in Event 2 at 03:00 UT hour for 21 keV particles. Particles traced in the Event 2 stayed longer than those of Event 1.

**Table 3.4**: Cusp events and their map onto different magnetospheric regions when backward particle tracing code runs Event based.

| | magnetosphere | magnetosheath | solar wind |
|---|---|---|---|
| Event 1 | 3 | 10 | 3 |
| Event 2 | 10 | 2 | 0 |

As presented in Table 3.6. and Table 3.7, out of 28 tracings, 13 were projected into magnetosphere and 12 into magnetosheath and 3 out to solar wind.

**Table 3.5**: Magnetospheric regions where the particle maps to at the end of the tracing

| Event1 | H | E (keV) | t (s) | Origin | Event2 | H | E (keV) | t (s) | Origin |
|---|---|---|---|---|---|---|---|---|---|
| | 3 | 21 | 5725 | Magnetosphere | | 3 | 21 | 7343 | Magnetosphere |
| | 3 | 27 | 2566 | Solar wind | | 3 | 27 | 2195 | Magnetosphere |
| | 3 | 1000 | 205 | Magnetosphere | | 3 | 1000 | 411 | Magnetosphere |
| | 3 | 3000 | 117 | Solar wind | | 3 | 3000 | 231 | Magnetosphere |
| | 4 | 21 | 1238 | Magnetosheath | | 4 | 21 | 4340 | Magnetosphere |
| | 4 | 27 | 1117 | Magnetosheath | | 4 | 27 | 4416 | Magnetosphere |
| | 4 | 1000 | 161 | Magnetosheath | | 4 | 1000 | 249 | Magnetosphere |
| | 4 | 3000 | 95 | Magnetosheath | | 4 | 3000 | 156 | Magnetosphere |
| | 5 | 21 | 1888 | Magnetosheath | | 5 | 21 | 6423 | Magnetosheath |
| | 5 | 27 | 1717 | Magnetosheath | | 5 | 27 | 4950 | Magnetosheath |
| | 5 | 1000 | 155 | Magnetosheath | | 5 | 1000 | 377 | Magnetosphere |
| | 5 | 3000 | 138 | Magnetosheath | | 5 | 3000 | 222 | Magnetosphere |
| | 6 | 21 | 4069 | Magnetosheath | | | | | |
| | 6 | 27 | 2144 | Magnetosheath | | | | | |
| | 6 | 1000 | 248 | Magnetosphere | | | | | |
| | 6 | 3000 | 64 | Solar wind | | | | | |

**Table 3.6:** Energetic particles and their projection onto the magnetospheric regions at the end of the particle tracing run.

| Projected to | Counts | 21 keV | 27 keV | 1 MeV | 3 MeV |
|---|---|---|---|---|---|
| Magnetosphere | 13 | 3 | 2 | 5 | 3 |
| Solar wind | 3 | 0 | 1 | 0 | 2 |
| Magnetosheath | 12 | 4 | 4 | 2 | 2 |

## 4. SUMMARY AND CONCLUSIONS

In the first part of this study, the BATS-R-US MHD results with INTERBALL spacecraft observations in the cusp region were compared. Two cusp crossings using energetic particle, magnetic field, plasma parameters were chosen. The BATS-R-US model which is available publicly on CCMC/NASA was run. Time series comparisons were made as the spacecraft moves through the cusp region from the magnetosphere into the solar wind in both events. The purpose in this part was to determine the model differences and the similarities, i.e. where, when and at what conditions the model agrees or disagrees with the observations, which in turn will help us to improve modeling. Comparisons also will help for understanding the observations better to explain our space environment and eventually will expand the understanding of physical and dynamic mechanisms on the solar wind magnetosphere coupling. The exercises carried out in this study and the results are very preliminary. Future analysis of the comparisons will continue. Below, results from the comparisons based on two events in the cusp region are listed.

1. In general, the model estimations were found to be much higher, Event 1, or lower, Event 2, than the observations although the amount of the difference is not the same for all parameters.

2. The best agreement was seen in the magnetic field. Qualitatively the model seems to catch the variations in the observed magnetic field in the cusp. Quantitatively predictions agree with the observations better when the IMF is northward than it is southward. During the southward IMF, the model predictions were found to be much smaller than the observed fields by a factor of 0.86.

3. Model predictions in density were found to be higher by a large amount and the variations in the model density are not consistent with the variations in observed density. Only a slight increasing tendency in density agrees with the observations. There is no dependence on IMF Bz in density comparisons as model is not successful in producing the features seen in the cusp in both IMF cases.

4. In velocity, model seems to work better quantitatively except that the high temporal fluctuations seen in the cusp were not caught by the model. On the average, model agrees with the observed velocity.

5. Differences between northward and southward IMFs can be attributable to the reconnection processes operating differently in both cases.

6. Model gives better agreement to observations in the exterior cusp than in the cusp.

In the second part of the study, a particle tracer code, which will be to examine the origin of the energetic particles in the cusp have been developed. This was a first step for this purpose and test runs were made and the code was found successfully working. Particle tracing code gave similar results to what is expected from the theory. One problem which needs more work on is to find a better way to interpolate the MHD outputs which come at the highest 4 min resolution to the position of the particle which moves at the gyro period, i.e. on the order of seconds/minutes. Therefore the results presented here as to the origin of the particles need care for interpretation. More detail analysis and work on more cases for particle tracing before moving on to determining the source of the energetic particles, which is still a controversial topic in the literature, will be done. The main purpose of this study was to show that the particle tracing code works. The code and its integration to the MHD model results to trace the particles in more realistic cases will be improved.

## REFERENCES


**Antonova, A.E., Gubar, Yu.I. and Kropotkin, A.P**., 2000. Energetic Particle Population in the High-Latitude Geomagnetosphere, *Phys. Chem. Earth*, Vol. **25**, No. 1-2, pp.47-50

**Chang, S.W**., **Scudder, J. D., Fuselier, S. A., Fennell, J. F., Trattner, K. J., Pickett, J. S., Spence, H. E., Menietti, J. D., Peterson, W. K., Lepping, R. P., and Friedel, R.** 1998. Cusp energetic ions: A bow shock source, *Geophys. Res. Lett.,* **25**, 3729

**Chen, J., Fritz T. A., Sheldon R. B., Spence H. E., Spjeldvik W. N., Fennell J. F., Livi S., Russell C. T., Pickett J. S., and Gurnett. D. A.** 1998. Cusp energetic particle events: Implications for a major acceleration region of the magnetosphere, *J. Geophys. Res.*, **103**, 69

**Chen, J. and Fritz, T.A.**, 1999. Features of the Cusp Energetic Particle Events, *adv. Space. Res.*, Vol. **24**, No. 1, pp. 103-107

**Decyk, V.K**., 1994. Description of Two Dimensional Particle Trajectory Code TRAJ2, Department of physics, UCLA

**Dungey, J. W.,** 1961. Interplanetary Magnetic Field and the Auroral Zones, Phys. Rev. Let., **6,** 47-49

**Farrell, W. M. and Van Allen J. A.**, 1990. Observations of the Earth's polar cleft at large radial distances with the Hawkeye 1 magnetometer, *J. Geophys. Res*., **95**, 20945-20958

**Fuselier, S.A., Berchman J., Trattner K.J., Friedel R.,** 2002. Tracing ions in the cusp and low-latitude boundary layer using multispacecraft observations and a global MHD simulation, *J. Geophys. Res.*, vol. **107**, No.A9, 1226

**Fritz, T.A., and Zong, Q.C.,** 2004. The Magnetospheric Cusp: A Summary, *Surveys in Geophysics*, **26,** 409-414

**Karra, M. and Fritz T. A.**, 1999. Energy dispersion features in the vicinity of the cusp, *Geophys. Res. Lett*., 26,

**Kaymaz, Z.,** 2006. Single Particle Motion, Space Environment Lecture Notes, Istanbul Technical University, Faculty of Aeronautics and Astromautics.

**Newell, P. T., Meng C. I., Sibeck D. G. and. Lepping R. P.**, 1989. Some low-altitude cusp dependencies interplanetary magnetic field, *J. Geophys. Res*., **94,** 8921-8927

**Omura, Y.**, 2005. One Dimensional Electromagnetic Particle Code, Proceedings of ISSS-7, 26-31 March

**Onsager, T. G., Chang, S.-W., Perez, J.D., Austin, J.B., and Jano, L.X.,** 1995. Low-altitude observations and modeling of quasi-steady magnetopause reconnection, *J. Geophys. Res.*, 100, 11,831

**Pissarenko, N.F., Kirpichev I.P., Lutsenko** V.N, 2001. Cusp Energetic Particles Observed by INTERBALL-Tail Probe in 1996, *Phys. Chem. Earth*, vol.**26**, no 1-3, pp. 241-245

**Raeder, J.**, 2003. Global Magnetohydrodynamics - A Tutorial in *Space Plasma Simulation*. *Lecture Notes in Physics, vol. 615*, pp.212-246, Eds. Büchner, J., Dum, C. and Scholer, M., Springer Verlag, Berlin

**Richard R. L., El-Alaoui M., Ashour-Abdalla, M., and Walker., R. J.,** 2002**.** Interplanetary Magnetic Field control of the entry of solar energetic particles into the magnetosphere, J. Geophys. Res., 107

**Russell, C.T.,** 2000. The Polar Cusp, *Adv. Space. Res*, **25(7/8)**, 1413-1424

**Sheldon, R. B., Spence, H.E., Sullivan, J., Fritz, T., and Chen, J.**, 1998. The Discovery of Trapped Energetic Electrons in the Outer Cusp, *Geophys. Res. Lett.*, **25**, 1825

**Simunek, J., Nemecek, Z., and Šafránková, J.**, 2003. Configuration of the Outer Cusp after an IMF Rotation, *Adv. Space. Res.,* vol.31, No.5, pp.1935-1400

**Toth, G., Volberg, O., Ridley, A. J., Gombosi, T. I. de Zeeuw, D., Hansen, K. C., Chesney, D. R., Stout, Q. F., Powell, K. G., Kane, K. J.; Oehmke, R. C.**, 2005. A Physics-Based Software Framework for Sun-Earth Connection Modeling in *Multiscale Coupling of Sun-Earth Processes,* p.383, Eds Liu, A. T. Y., Kamide, Y. and Consolini, G., Elsevier B. V.; Amsterdam, The Netherlands

**Tsyganenko, N. A**., 1989a. A solution of the Chapman-Ferraro problem for an ellipsoidal magnetopause, Planet. Space Sci., **37**, 1037-1046

**Tsyganenko, N. A**., 1989b. A magnetospheric magnetic field model with a warped tail current sheet, Planet. Space Sci., **37,** 5-20

**Zhou, X. W., Russell, C. T., Fuselier., Le, G., S. A and Scudder, J. D**. 1999. The Polar Cusp Location and its Dependence on Dipole Tilt, *Geophys. Res. Lett.*, **26**, 3

**Zhou, X. W., Russell, C.T., Le, G., Fuselier S.A., Scudder, J.D.**, 2000. Solar Wind Control of the Polar Cusp at High Altitude*, J. Geophys. Res.*, **105**, 245-251

[1]. **Oulu Space Physics Textbook**, [01.07.2007]

http://www.oulu.fi/~spaceweb/textbook/

[2]. **Coordinated Data Analysis Web**, [01.07.2007]. http://cdaweb.gsfc.nasa.gov/ .

**BIOGRAPHY**

Born in Ulaanbaatar, Mongolia on 5th November 1981.

**Education**

| | |
|---|---|
| 1989-1996 | The 24th school in Chingeltei district, Ulaanbaatar, Mongolia |
| 1996-1999 | Mongolian-Turkish high school, Ulaanbaatar, Mongolia |
| 1999-2000 | Turkish preparatory class, TÖMER, Izmir, Turkey |
| 2000-2005 | Bachelor degree in Meteorological Engineering, Istanbul Technical University, Istanbul, Turkey<br>Bachelor degree in Physical Engineering, Istanbul Technical University, Istanbul, Turkey |
| 2005-2007 | awaiting Masters degree in Meteorological Engineering, Istanbul Technical University, Istanbul, Turkey |

**Scholarships**

| | |
|---|---|
| 1999-2005 | Turkish Government undergraduate scholarship |
| 2005-2007 | Turkish Government graduate scholarship |

**Internships**

| | |
|---|---|
| Summer, 2003 | Istanbul Metropolitan Municipality, Air pollution Unit, Air pollution internship |
| Summer, 2004 | Göztepe Meteorology station, Climatologic internship |
| Summer, 2005 | Atatürk Airport, Office of Weather Forecast and Analysis, Synoptic internship |

**Language skills**

| | |
|---|---|
| Mongolian | Mother Tongue |
| Turkish | advanced |
| English | advanced |
| German | intermediate |
| Russian | beginner |